

# Structural basis for regulation of CELSR1 by a compact module in its extracellular region

Received: 21 February 2024

Accepted: 17 April 2025

Published online: 28 April 2025



Sumit J. Bandekar<sup>1,2,3,4</sup>, Krassimira Garbett<sup>5</sup>, Szymon P. Kordon<sup>1,2,3,4</sup>, Ethan E. Dintzner<sup>1,2,3,4</sup>, Jingxian Li<sup>1,2,3,4</sup>, Tanner Shearer<sup>5</sup>, Richard C. Sando<sup>5</sup>✉ & Demet Araz<sup>1,2,3,4</sup>✉

The Cadherin EGF Laminin G seven-pass G-type receptor subfamily (CELSR/ADGRC) is one of the most conserved among adhesion G protein-coupled receptors and is essential for animal development. The extracellular regions (ECRs) of CELSRs are large with 23 adhesion domains. However, molecular insight into CELSR function is sparsely available. Here, we report the 3.8 Å cryo-EM reconstruction of the mouse CELSR1 ECR and reveal that 14 domains form a compact module mediated by conserved interactions majorly between the CADH9 and C-terminal GAIN domains. In the presence of  $\text{Ca}^{2+}$ , the CELSR1 ECR forms a dimer species mediated by the cadherin repeats putatively in an antiparallel fashion. Cell-based assays reveal the N-terminal CADH1-8 repeat is required for cell-cell adhesion and the C-terminal CADH9-GAIN compact module can regulate cellular adhesion. Our work provides molecular insight into how one of the largest GPCRs uses defined structural modules to regulate receptor function.

Multicellular organisms use an array of cell-surface receptors to facilitate productive adhesion between cells and initiate events to control developmental and regulatory processes. The adhesion class of G protein-coupled receptors (aGPCRs) is an understudied family of cell-surface receptors that link adhesion to intracellular events through their multidomain extracellular regions (ECRs)<sup>1–3</sup>. The aGPCR subfamily of Cadherin epidermal growth factor (EGF) Laminin G seven-pass G-type receptors (CELSRs or ADGRCs) is one of two aGPCR subfamilies conserved as distantly as *C. elegans* and CELSRs are essential for the embryonic and neural development of animals<sup>4–7</sup>. There are three mammalian CELSRs (CELSR1–3) and other commonly studied orthologs include *C. elegans* Flamingo (Fmi) and *D. melanogaster* Starry Night (Stan)/Flamingo (Fmi)<sup>6</sup>. CELSRs are involved in the process of planar cell polarity (PCP)<sup>8–13</sup>, where they are key for neural tube closure<sup>8,10,14,15</sup>, organization of inner ear stereocilia<sup>8,10</sup>, neuroepithelial cilia<sup>16</sup>, lymphatic valve formation<sup>17</sup>, and skin hair patterning<sup>8,15</sup>. In the nervous system, CELSRs regulate neuronal migration, dendritic growth, axon guidance, and

glutamatergic synapse formation<sup>18–23</sup>. CELSRs are ubiquitously expressed in epithelial cell types during embryonic development<sup>24–27</sup>. During the development of the nervous system, CELSRs are highly expressed throughout the central nervous system (CNS)<sup>24–26</sup>. Mutations in CELSRs are strongly associated with neural tube defects, including spina bifida and craniorachischisis, resulting in a range of physical and intellectual disabilities up to embryonic lethality<sup>28–32</sup>. CELSRs are also associated with lymphedema, Joubert syndrome, Tourette syndrome, fetal hydrops, and the progression of leukemia<sup>33–41</sup>.

From their N-termini, CELSRs have poorly conserved prodomains (PRO) with a putative furin cleavage site. Following PRO are nine cadherin repeats (CADH1–9) which take up ~40 % of the ECR mass, making CELSRs a unique CADH-containing subfamily of the aGPCRs<sup>42–44</sup>. Cadherin repeats are protein-protein interaction (PPI) modules with ~100 residue globular domains with linker regions that coordinate calcium. Three  $\text{Ca}^{2+}$  ions bind between two CADH repeats and rigidify this linker, and this can include many repeats in tandem.

<sup>1</sup>Department of Biochemistry and Molecular Biology, The University of Chicago, Chicago, IL, USA. <sup>2</sup>The University of Chicago Neuroscience Institute, The University of Chicago, Chicago, IL, USA. <sup>3</sup>Institute for Biophysical Dynamics, The University of Chicago, Chicago, IL, USA. <sup>4</sup>Center for Mechanical Excitability, The University of Chicago, Chicago, IL, USA. <sup>5</sup>Department of Pharmacology, Vanderbilt Brain Institute, Vanderbilt University, Nashville, TN, USA.

✉ e-mail: [Richard.sando@vanderbilt.edu](mailto:Richard.sando@vanderbilt.edu); [arac@uchicago.edu](mailto:arac@uchicago.edu)

This rigid CADH repeat structure mediates cell adhesion in a specific manner<sup>45,46</sup>. CADH repeats act as “molecular Velcro” to hold cells together and are mechanotransducers<sup>47</sup>. CELSR1 mutants which change single CADH residues directly involved in coordinating  $\text{Ca}^{2+}$  result in PCP phenotypes and embryonic lethality<sup>8</sup>. Following the CELSR cadherin repeats, there is a Flamingo box (FBox) domain, which is unique to CELSR/Fmi proteins<sup>13</sup>. FBox domains bear structural homology to the membrane-adjacent domains (MADs) of protocadherins (pCDHs)<sup>48</sup>. Furthermore, CELSRs have a similar domain architecture to pCDHs and FAT cadherins, which have a series of CADH repeats, a MAD domain, and either a transmembrane domain (pCDH) or a series of LamG and EGF domains (FAT)<sup>42,44,48–50</sup>. pCDHs overlap several N-terminal CADH repeats to dimerize, making tight antiparallel dimers which can serve as mechanotransducers; these proteins are also involved in neuronal self-avoidance<sup>51–56</sup>. MADs can form cis-dimers with an adjacent CADH repeat, where the minimal unit of N-CADH-MAD-C is necessary to dimerize<sup>48</sup>. Multiple studies have demonstrated the importance of the CELSR CADH region in cell adhesion, but molecular detail is sparsely available<sup>11–13,20</sup>. The only available information comes from a recent structural study, which determined low-resolution images of the full ECR of human CELSR2, showing an extended region likely consisting of the CADH repeats, and a globular region of unknown structure. This study also shows that the CADH repeats likely wrap around each other tightly, using multiple cadherin domains to form tight extended dimer species similar in principle to protocadherins<sup>57</sup>. Another recent study determined crystal structures of monomeric CELSR1 CADH1-4 and CADH4-7, giving the first high-resolution insight into the CADH repeat region of CELSR and revealing a non-canonical linker between CADH5 and CADH6<sup>58</sup>.

Next, CELSRs have a series of EGF and Laminin G (LamG) domains. CELSR1 has 3 EGF repeats (EGF1-3), the first LamG domain (LamG1), EGF4, LamG2, and EGF5-8. EGF repeats found extracellularly can serve scaffolding functions<sup>59–63</sup> or act as PPI modules<sup>64</sup>. LamG domains are found in PPI sites, such as in Neurexin<sup>65,66</sup>. The ECR ends with the hormone receptor (HormR) and GPCR autoproteolysis-inducing (GAIN) domains. CELSR orthologs across different species variably include the residues for GAIN domain autoproteolysis<sup>67,68</sup>. In *D. melanogaster* Fmi, the EGF/LamG/HormR/GAIN region plays a role in the interaction with Frizzled, an Fmi binding partner involved in PCP<sup>69</sup>, but no function for this region has been demonstrated for vertebrate CELSRs. At their C-terminus, CELSRs have a seven transmembrane (7TM) region and a long intracellular region of about 300 residues.

Despite various hints of CELSR structure and function available in the literature, detailed information at the molecular level about these proteins is minimally present. In addition, the mechanistic insight into how CELSRs receive adhesion as an extracellular cue and process it remains unavailable. In this work, we determined the 3.8 Å cryogenic electron microscopy (cryo-EM) reconstruction of the CELSR1 ECR, which revealed a compact multidomain module (CMM) consisting of fourteen domains, including CADH9-GAIN. Within this CMM, the N-terminal CADH9 and C-terminal GAIN domain form the primary contact interface using conserved residues. We also report the experimental structure of the FBox domain within this module. We used biophysical assays to study the full ECR in the presence of  $\text{Ca}^{2+}$ , and we observed an extended species, which we propose represents an intertwined antiparallel dimer found in a configuration similar to protocadherins. We analyzed truncations of CELSR1, and we show that the CADH1-8 module is sufficient for cellular adhesion. Finally, we show that point mutations in the CADH9/GAIN interface led to increased cell aggregation activity. Other aGPCRs have CMMs and therefore the CMM may represent a paradigm for regulating aGPCR function, which maintains specific distance restraints, allows regulation by splice variation, or is sensitive to mechanical force.

## Results

### Cryo-EM reveals that CADH9-GAIN forms a compact module

We purified the CELSR1 ECR construct containing domains from CADH1-GAIN (Fig. 1a, Supplementary Fig. 1a–c), and we performed single-particle cryo-EM analysis on this construct. Our initial 2D class averages from screening images showed compact triangle-shaped particles about 160 Å in the longest dimension (Supplementary Fig. 1d, e). Processing of a full dataset resulted in a 3.8 Å reconstruction (Fig. 1b, Table 1, and Supplementary Figs. 2 and 3) which allowed for unambiguous assignment of the CADH9-GAIN domains within the density map (Fig. 1c). The CADH1-8 domains are unresolved in this reconstruction; presumably they are flexible relative to the CADH9-GAIN module in the absence of  $\text{Ca}^{2+}$ . They appear in 2D averages as blurry density connected to CADH9 (Supplementary Fig. 2c). The fourteen domains in the CADH9-GAIN module form a CMM architecture reminiscent of the ouroboros, an ancient symbol of rebirth where a snake is depicted eating its own tail<sup>70</sup>. The overall dimensions are around 160 × 120 × 75 Å. CADH9 forms the “head” of the snake (Fig. 1c), and the GAIN domain is the “tail.” The CADH9/GAIN interaction surface plays a critical role in stabilizing the module (Fig. 1c). CADH9, FBox, EGF1-3, and LamG1 are tightly packed next to each other, occluding the putative LamG1 binding site<sup>71</sup>. EGF4 and LamG2 also form a compact group, with the LamG2 putative ligand binding site<sup>71</sup> accessible for binding partners. Then, EGF5-8 are found in an extended conformation, representing the long body of the snake wrapped around the other domains. EGF6 contacts LamG1, and EGF7 contacts EGF2. Finally, EGF8 leads into the HormR domain and the GAIN domain.

Our cryo-EM reconstruction allows us to report the experimental structure of the FBox domain, a domain type thought to be unique to CELSR/Flamingo orthologs (Supplementary Fig. 4a)<sup>13</sup>. We confirm previous work which predicted the FBox domain to be structurally similar to MAD domains of protocadherins and FAT cadherins, as well as the ferredoxin-like domains of nuclear pore proteins<sup>48,72</sup>. Using the DALI webserver, we identified several SEA domains as structural homologs of FBox, including SEA of the aGPCR ADGRG6 (Supplementary Fig. 4a)<sup>73</sup>. The CELSR FBox domain does not have the residues for furin cleavage, which some SEA domains have (Supplementary Fig. 4b)<sup>74</sup>. The pCDH15 MAD domain forms a dimer with its adjacent CADH repeat, where the CADH of one monomer interacts with the MAD of the other monomer, and vice versa. The orientation of CADH9 to FBox is different from the CADH11-MAD orientation in pCDH15, and the dimerization surface is sterically hindered within the CELSR CMM (Supplementary Fig. 4c, d).

We can hypothesize how the CADH9-GAIN module is oriented relative to the membrane using our structure supplemented with AlphaFold2 models (Supplementary Fig. 4e, f)<sup>75</sup>. A large loop in the GAIN domain, which is basic and hydrophobic, could transiently interact with the outer surface of the membrane. Surfaces on EGF2/3, EGF8, and HormR also have surface-exposed hydrophobic patches facing the putative plasma membrane. With this orientation, the flat plane of the CADH9-GAIN module is angled about 30° from the plasma membrane, and the cadherin repeats would project outward at that angle.

### The CADH9-GAIN module is stabilized by interdomain contacts

Three key interfaces stabilize the CADH9-GAIN module (Fig. 2a, Supplementary Fig. 5, Supplementary Table 1). In the CADH9/GAIN interface (Fig. 2b), conserved residues F2188 and Y2250 interact with L1163, L1165, and L1187. Additionally, N1184 and R1185 from CADH9 interact with several residues on GAIN. Additional residues are involved, and this interface buries ~1100 Å<sup>2</sup> from solvent. Hydrophobic contacts are also seen between EGF2 and EGF7, burying ~470 Å<sup>2</sup> from solvent (Fig. 2c). I1379 and Y1383 of EGF2 pack against W1972, W1973, V1977, and P1980 of EGF7. A robust hydrophobic core is observed between

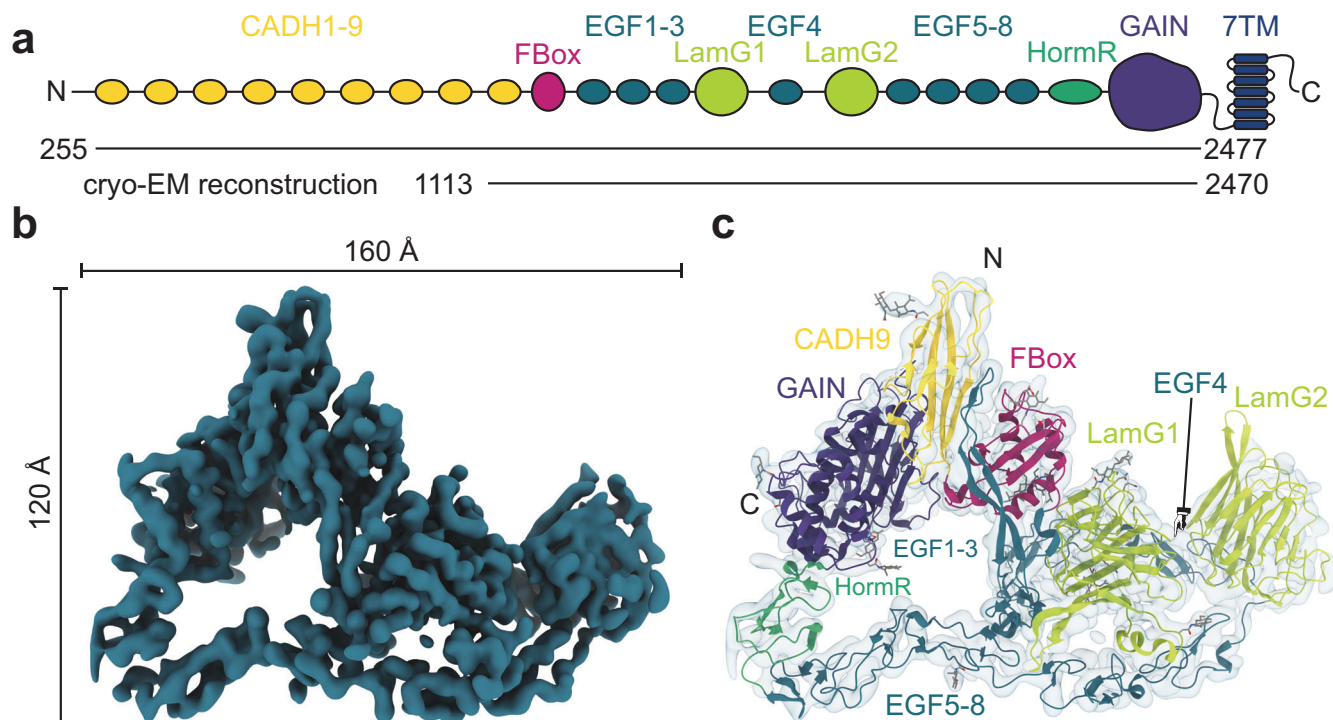


**Fig. 1 | The 3.8 Å Cryo-EM reconstruction of the extracellular region of CELSR1 reveals a compact interdomain bundle including 14 domains. a** A cartoon diagram shows the overall domain architecture of CELSR1 with horizontal lines indicating boundaries used in the construct and the boundaries resolved in the reconstruction. CADH cadherin repeat (yellow oval), FBox Flamingo Box domain (pink oval), EGF epidermal growth factor repeat (teal oval), LamG laminin G repeat (lime green oval), HormR hormone receptor domain (green oval), GAIN GPCR

autoproteolysis-inducing domain (purple shape), 7TM seven transmembrane region (blue cylinders), ICR intracellular region. **b** Coulomb potential map of the cryo-EM reconstruction, colored in dark teal, reveals a compact triangular shape. **c** A cartoon representation of the CELSR1 ECR atomic model, colored as in (a), fit into the Coulomb potential map shows that the N-terminal portion of the structure interacts with the C-terminal portion.

LamG1 and EGF6, burying  $\sim 770 \text{ \AA}^2$  from solvent (Fig. 2d). Residues V1581, F1585, Y1588, and V1589 from LamG1 pack against F1918, V1923, P1930, and Y1947 from EGF6. Also, D1578 interacts with the hydroxyl of Y1947.

### CELSR1 forms a $\text{Ca}^{2+}$ -dependent dimer with an extended conformation

We did not observe the CADH1-8 domains in our cryo-EM reconstruction, even though these domains were about 40 % of the mass of our CELSR1 construct. CADH repeats have flexible interdomain linkers that rigidify upon  $\text{Ca}^{2+}$  binding, forming extended species that multimerize<sup>45,46</sup>. In order to resolve the CADH repeats, we biophysically characterized the CADH1-GAIN construct in the absence and presence of  $\text{Ca}^{2+}$  using inline size exclusion chromatography coupled to multiangle light scattering and small-angle X-ray scattering (SEC-MALS-SAXS) (Fig. 3, Supplementary Data 1 and 2). We observed a leftward shift in the elution volume in the presence of 1 mM  $\text{CaCl}_2$  (Fig. 3a) and an increase in observed molecular mass by MALS, suggesting that the protein forms a dimer in solution. In the 1 mM  $\text{CaCl}_2$  condition, the main peak is likely a mixture of a dimer and a monomer due to its MALS molecular weight of 420 kD, which corresponds to roughly 60% dimer ( $\sim 520$  kD) and 40 % monomer ( $\sim 260$  kD) (Fig. 3a).

Using evolving factor analysis (EFA) deconvolution techniques, we separated individual scattering components from the SEC-SAXS curves and derived electron density reconstructions for these species (Fig. 3b–e and Supplementary Data 1, 2). We separated out the scattering for the monomer species (Supplementary Data 1 and 2) and found that a density map for the no  $\text{CaCl}_2$  condition corresponds well in overall shape with the cryo-EM Coulomb potential map with similar dimensions at  $\sim 220 \times 140 \times 120 \text{ \AA}$  (Fig. 3b, c), suggesting that the CADH9-GAIN CMM is present in solution. We used EFA to separate out

the scattering from the dimer component in the 1 mM  $\text{CaCl}_2$  condition (Supplementary Data 1 and 2). We then generated an electron density map and found that the dimer component is overall extended at  $\sim 500 \times 220 \times 220 \text{ \AA}$  (Fig. 3d, e), and we propose that this overall extended shape corresponds to CADH1-8 in an antiparallel configuration (Fig. 3f), similar to that reported from atomic force microscopy<sup>57</sup>. A model of the entire CELSR ECR in this antiparallel configuration (Fig. 3f) could range from roughly 500–600 Å in maximum dimensions, depending on the curvature of the CADH repeats. This is in overall agreement with the 1 mM  $\text{CaCl}_2$  dataset as it has a pairwise distance distribution function with  $D_{\text{max}} = 675 \text{ \AA}$  and a small peak  $\sim 520 \text{ \AA}$  (Supplementary Data 1 and 2).

### MD simulations support a hinge region between CADH5-6

Using the deposited crystal structure of human CELSR1 CADH4-7, we investigated the dynamics of the proposed hinge region within the cadherin repeat region of CELSR<sup>57,58</sup>. In CELSR1, K533 and T564 between CADH5 and CADH6 are non-canonical. In other cadherin repeat proteins, these positions are typically acidic calcium-coordinating residues. These substitutions prevent the coordination of two out of three  $\text{Ca}^{2+}$  ions usually found between cadherin repeats. We performed three MD simulations (Fig. 4a and Supplementary Fig. 5e), one with the wild-type CADH4-7 (WT), another where all calcium ions in the CADH5/CADH6 hinge were deleted ( $\Delta\text{Ca}^{2+}$ ), and a third where the non-canonical calcium-coordinating residues were changed to the canonical ones, K533E/T564D, and  $\text{Ca}^{2+}$  ions were added manually (Canonical). We analyzed bending angles between CADH5 and CADH6 throughout each simulation and found that while the Canonical simulation remained close to  $180^\circ$  for the 100 ns simulation, both the WT and  $\Delta\text{Ca}^{2+}$  simulations diverged from this and displayed bending after 50 ns. We performed principal component (PC) analysis

**Table 1 | Cryo-EM data collection and processing statistics**

	CELSR1 ECR Data-set A	CELSR1 ECR Data-set B
<b>Data collection and processing</b>		
Magnification (x)	81,000	81,000
Voltage (kV)	300	300
Electron Exposure (e <sup>-</sup> /Å <sup>2</sup> )	50	50
Exposures	5826	5550
Defocus range (μm)	-1.0 to -2.0	-0.7 to -1.7
Pixel Size (Å)	0.55	0.55
Symmetry Imposed	C1	C1
<b>Reconstruction</b>		
Initial Particle images	4,964,141	
Final Particle images	275,998	
Global Resolution (Å)	3.8	
Resolution Range (Å)	2.4–6.0	
Map Sharpening B factor (Å <sup>2</sup> )	-193	
<b>Model composition</b>		
Non-hydrogen atoms	10,374	
Protein Residues	1319	
Ligands	15	
<b>B factors</b>		
Protein (Å <sup>2</sup> )	270	
Ligand (Å <sup>2</sup> )	271	
<b>R.M.S. deviations</b>		
Bond lengths (Å)	0.005	
Bond Angles (°)	0.908	
<b>Validation</b>		
MolProbity Score	2.11	
Clashscore	13	
Poor rotamers (%)	0.97	
<b>Ramachandran plot</b>		
Favored (%)	91.94	
Allowed (%)	7.6	
Disallowed (%)	0.46	

on these simulations and performed unbiased hierarchical clustering in the PC space (Fig. 4b). After obtaining three clusters (Clusters A–C), we examined frames of the simulation near the centroid of each cluster to understand the conformational dynamics (Fig. 4c). In Cluster A, the molecule is bent to ~100° about the CADH5/CADH6 linker region. Cluster B is represented by a ~135° bend in the CADH5/CADH6 linker. Cluster C corresponds to an approximately linear configuration (180°). We quantified the percentage of time that each variant spent in each cluster (Fig. 4d) and found that the WT and ΔCa<sup>2+</sup> simulations can flex about the CADH5/6 hinge and sample both extended and bent conformations. However, these two simulations spend the majority of their time in bent conformations (Clusters A and B). In contrast, the Canonical simulation is largely limited to the extended conformation (Cluster C). Another group studying CELSR1 using molecular dynamics also observed similar bending movements about CADH5/CADH6<sup>58</sup>. Furthermore, bending of the CELSR ECR in a manner consistent with our observations has been observed using atomic force microscopy<sup>57</sup>, this behavior has been reported for other cadherins<sup>76,77</sup>, and these results are consistent with the literature on cadherin biochemistry and structure<sup>45,78</sup>.

### CADH1-8 are essential for the adhesive functions of CELSR1

To address which portions of CELSR1 contribute to its adhesive and signaling functions, we split the protein into two modules according to

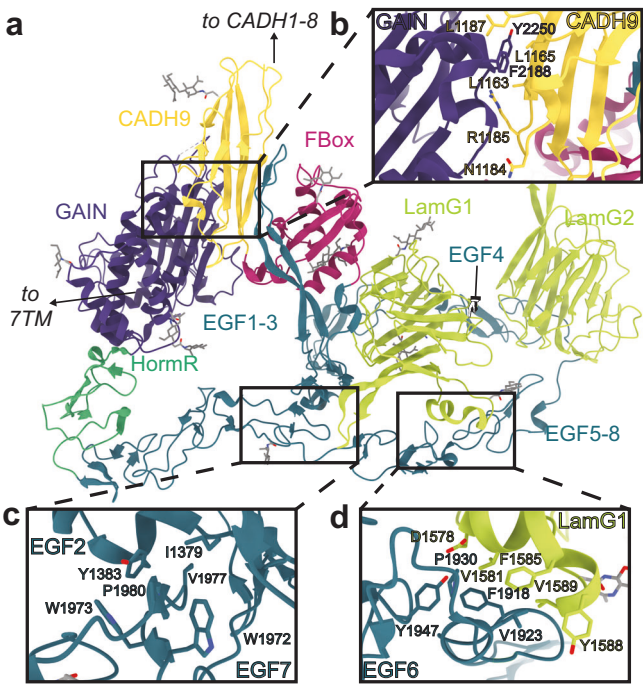


**Fig. 2 | Structural details of interdomain interfaces stabilizing the CELSR1 ECR compact bundle. a** Cartoon representation of CELSR1 ECR structure with key interfaces enclosed in black rectangles. CADH cadherin repeat (yellow), FBox Flamingo Box domain (pink), EGF epidermal growth factor repeat (teal), LamG laminin G repeat (lime green), HormR hormone receptor domain (green), GAIN GPCR autoproteolysis-inducing domain (purple), 7TM seven transmembrane region. **b** Cartoon model showing the interface between CADH9 and GAIN domains. Important residues are shown as sticks. **c** Cartoon model showing the interface between EGF2 and EGF7 domains with important residues shown as sticks. **d** Cartoon model showing the EGF6/LamG1 interface with important residues shown as sticks.

our structural information. We deleted the CADH1-8 module (ΔCADH1-8) as well as the CMM resolved in our structure (ΔCADH9-GAIN) (Fig. 5a). We tested the expression of our constructs using fluorescence microscopy (Fig. 5b–d) and western blotting (Supplementary Fig. 6a–c, Supplementary Methods) and used their relative cell-surface expression levels to normalize further experiments. We then profiled the adhesive function of our constructs in cell aggregation assays as well as a cell-cell junction enrichment assay. In the cell aggregation assay, each full-length protein is expressed in two different HEK293T cell populations, and a fluorescent reporter is co-expressed. The cells are then mixed, and cell-cell aggregation is imaged and quantified<sup>79</sup>. WT CELSR1 was able to efficiently induce aggregation (Fig. 5e–g), the ΔCADH1-8 construct was defective in aggregation, and the ΔCADH9-GAIN construct was able to form aggregates but not as efficiently as WT. In the cell-cell junction enrichment assay, full-length protein is expressed using HEK293T cells observed in groups, and the localization of CELSR1 is compared to ZO-1, a cell-cell junction marker<sup>80,81</sup>. Similar to the results for the cell aggregation assay, in the cell-cell junction assay, WT CELSR1 efficiently localized to the cell-cell junction (Fig. 5h–j), whereas the ΔCADH1-8 construct was found distributed all over the cell surface and not only at the cell-cell junction. The ΔCADH9-GAIN construct is also localized to the cell-cell junction. We thus report the CADH1-8 module as sufficient for cell-cell adhesion. Neither deletion construct affected CELSR1 signaling activity (Supplementary Fig. 6d, e).

We also found that WT CELSR1-mediated aggregation was abolished in the presence of EGTA, a selective Ca<sup>2+</sup> chelator (Supplementary Fig. 6f–h) whereas aggregation mediated by TEN2/ADGRL3 was not affected by EGTA, serving as a control<sup>60</sup>. Finally, we found

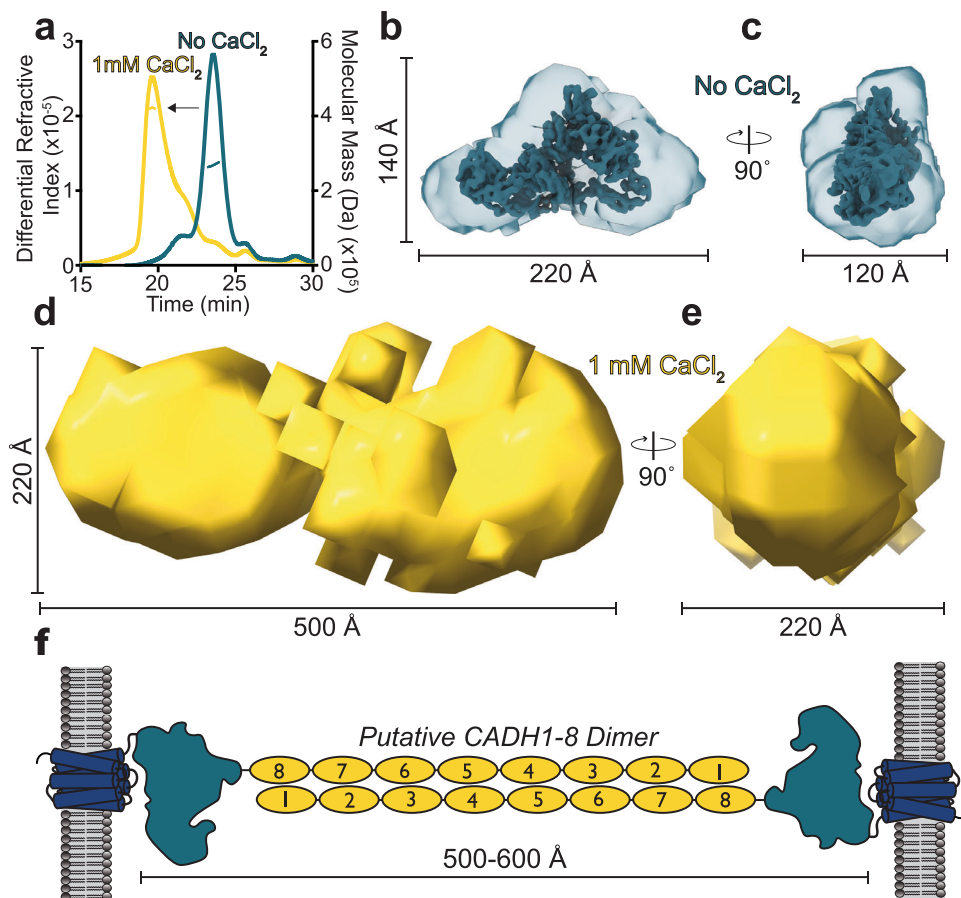


**Fig. 3 | SEC-MALS-SAXS analysis of CELSR1 CADH1-GAIN.** **a** Overlay of SEC-MALS traces in the absence of  $\text{CaCl}_2$  (dark teal curve) and in the presence of 1 mM  $\text{CaCl}_2$  (yellow curve). A leftward shift of the elution volume is seen with 1 mM  $\text{CaCl}_2$ , suggesting the presence of a  $\text{Ca}^{2+}$ -dependent dimer. Differential refractive index is plotted on the left, and the calculated molecular mass is plotted on the right axis. The traces represent the differential refractive index, whereas the horizontal lines in the peaks show the calculated molecular masses. **b** An electron density map generated using DENS based on the No  $\text{CaCl}_2$  SAXS curve agrees well with the cryo-EM Coulomb potential map, suggesting that the CADH9-GAIN CMM exists in solution. Both maps are colored in dark teal. **c** An orthogonal view shows that the

overall shape of the density is flat in one dimension relative to the other two. **d** A density map generated using DENS based on the 1 mM  $\text{CaCl}_2$  SAXS curve shows a large, extended structure longer in one dimension. The density map is colored yellow. **e** Orthogonal view of **(d)**. **f** A cartoon diagram with a hypothesis for how the CADH repeat region (yellow) is linked to the CMM (dark teal) and the 7TM (blue) is arranged within the extended density observed in **(d, e)**. The model can extend from 500 to 600 Å, depending on the curvature of the cadherin repeats. The density in **(d, e)** has a maximum of 500 Å in its longest dimension, whereas the 1 mM  $\text{CaCl}_2$  dataset has a pairwise distance distribution function with  $D_{\text{max}} = 675$  Å. Source data are provided as a Source Data file.

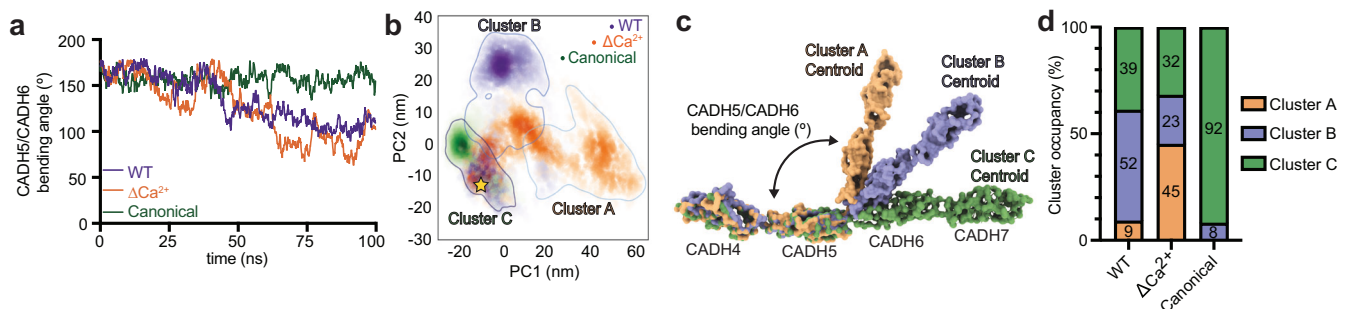


**Fig. 4 | Molecular dynamics simulations on hCELSR1 CADH4-7 support that a flexible hinge exists between CADH5 and CADH6.** **a** Plot of CADH5/CADH6 bending angle over time for each simulation (WT—purple,  $\Delta\text{Ca}^{2+}$ —burnt orange, Canonical—green). **b** Kernel density estimates of each simulation plotted onto PC space. A yellow star shows the start point of each simulation. Clustering of

conformations in essential principal component space reveals three clusters, labeled as clusters A–C. **c** Each shown PDB model is a frame of the simulation that is closest to the centroid of the designated cluster. **d** The percentage of simulation time that each simulation spends in each cluster. Each simulation was performed in  $N=1$  for a total time of 100 ns. Source data are provided in the Source Data file.

that CELSR1 and CELSR2 can form heterophilic aggregates when two cell populations expressing these proteins are mixed, and this effect is also disrupted by EGTA supplementation (Supplementary Fig. 6f–h).

### Mutations in the CADH9/GAIN interface enhance cellular adhesion

In order to understand the role of the CADH9-GAIN CMM in modulating CELSR function, we designed point mutations in the interface

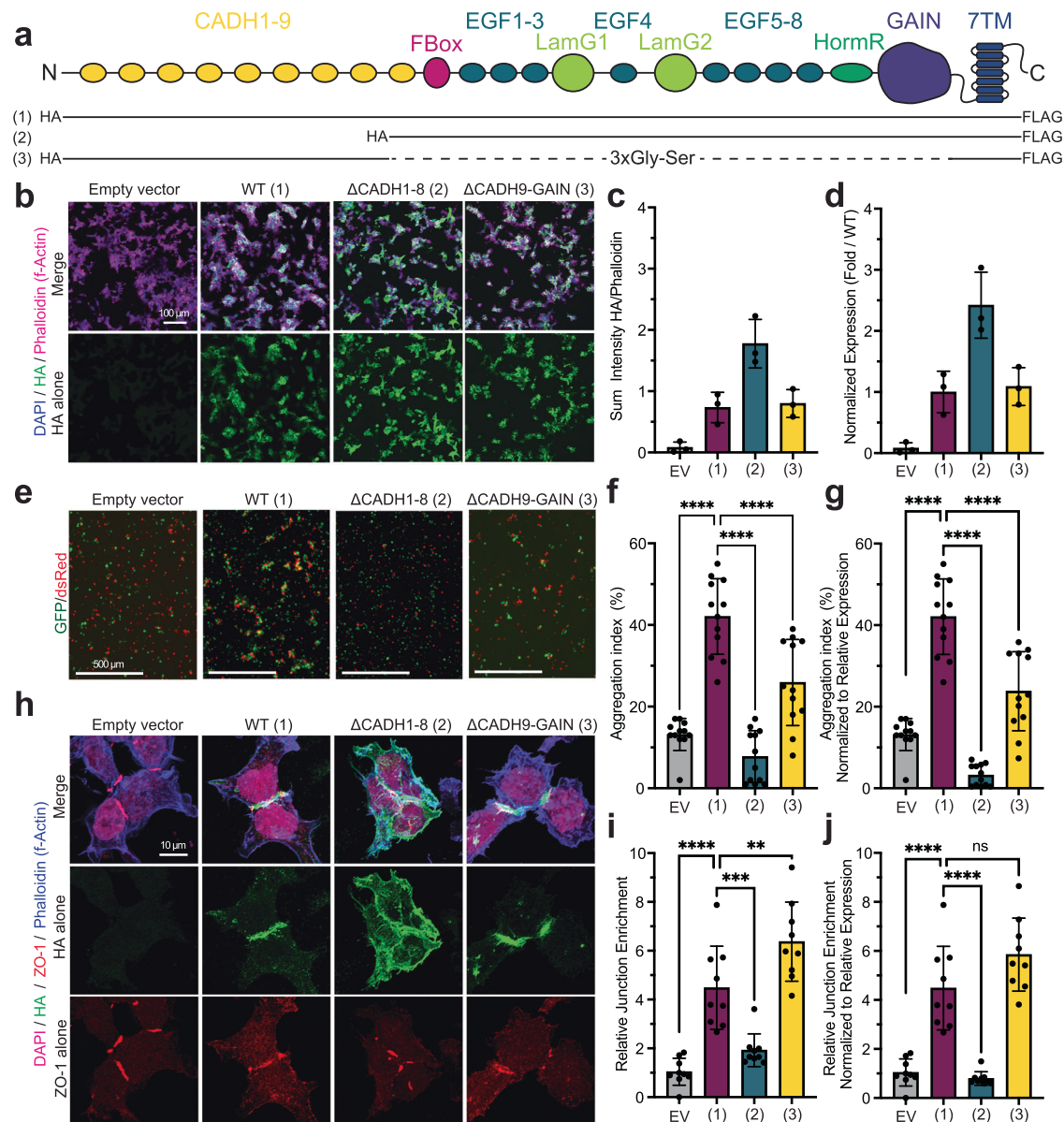


**Fig. 5 | Functional analysis of the adhesive properties of the CELSR1 ECR.**

**a** Domain boundaries of constructs used in this study. CADH cadherin repeat (yellow oval), FBox Flamingo Box domain (pink oval), EGF epidermal growth factor repeat (teal oval), LamG laminin G repeat (lime green oval), HormR hormone receptor domain (green oval), GAIN GPCR autoproteolysis-inducing domain (purple shape), 7TM seven transmembrane region (blue cylinders), ICR intracellular region. Black solid lines show domain boundaries, with dotted lines indicating regions that are connected with linkers. **b** Experimental constructs were tested for cell-surface expression using non-permeabilized cells imaged using the N-terminal HA tag (green). DAPI marks the nucleus (blue), and phalloidin marks filamentous actin (pink). Representative images are shown. **c** The ratio of HA/Phalloidin intensity is used to quantify relative cell-surface expression of each truncation construct. Each point represents one independent biological replicate and is the average of 3 technical replicates. Error is shown as the standard deviation from the mean. pEB, gray; WT CELSR1, purple; ΔCADH1-8, teal; ΔCADH9-GAIN, yellow. **d** The relative cell surface expression of each construct is presented as a fold change over wild type, points, error, and color are as in (c). **e** Representative cell-cell aggregation assay images. Two cell populations were transfected with either GFP or dsRed and the noted constructs, and cells were imaged to assess aggregation. **f** Quantification of cell aggregation images as aggregation index.  $N = 3$  independent

biological replicates, each with 4 technical replicates; each technical replicate is shown as a data point. The average is plotted as a bar graph with standard deviation shown for the error bars. pEB, gray; WT CELSR1, purple; ΔCADH1-8, teal; ΔCADH9-GAIN, yellow. **g** Quantification of aggregation index normalized to the relative cell surface expression of each construct, points, error, and color are as in (f). **h** Representative cell-cell junction enrichment assay images. Experimental constructs were imaged using the N-terminal HA tag (green). ZO-1 is used as a marker for the cell-cell junction (red), DAPI for the nucleus (pink), and phalloidin for filamentous actin (blue). **i** Quantification of images from (h) as relative junction enrichment.  $N = 3$  independent biological replicates, each done with three technical replicates; each technical replicate is shown as a data point; the average is plotted as a bar graph with standard deviation shown for the error bars. pEB, gray; WT CELSR1, purple; ΔCADH1-8, teal; ΔCADH9-GAIN, yellow. **j** Quantification from (i) normalized to relative cell surface expression of each construct, points, error, and color are as in (i). One-way ANOVA with Tukey's correction for multiple comparisons was performed to assess statistical significance between CELSR constructs in (f, g, i, j). \*\* corresponds to  $p = 0.0085$ , \*\*\* corresponds to  $p = 0.0004$ , \*\*\*\* corresponds to  $p < 0.0001$ . Each construct was compared to each other construct for the statistical testing, but only certain comparisons are shown for clarity. Source data are provided as a Source Data file.

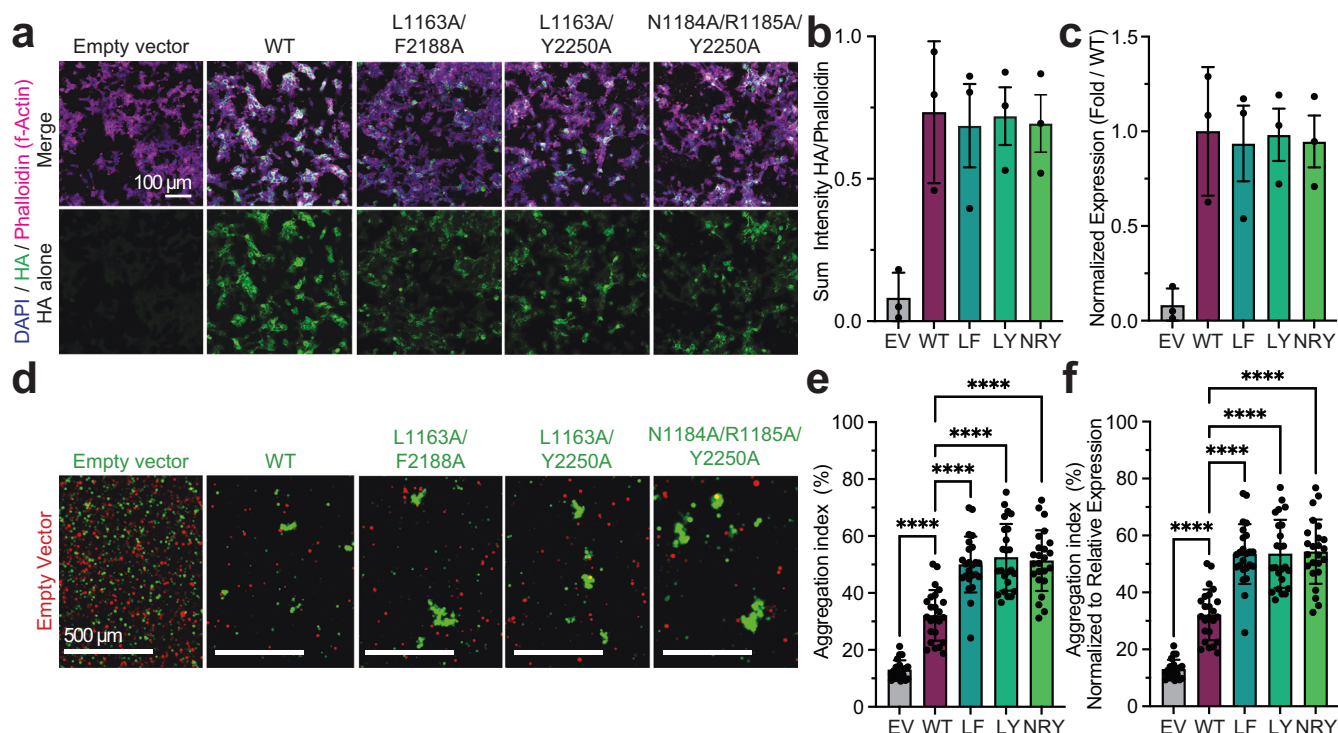


**Fig. 6 | Point mutations in the CADH9/GAIN interface enhance CELSR1-mediated cell aggregation.** **a** Experimental constructs were tested for cell-surface expression using non-permeabilized cells imaged using the N-terminal HA tag (green). DAPI marks the nucleus (blue), and phalloidin marks filamentous actin (pink). Representative images shown. **b** The ratio of HA/Phalloidin intensity is used to quantify cell-surface expression of each construct, each point represents one independent biological replicate and is the average of three technical replicates. Error is shown as the standard deviation from the mean. LF L1163A/F2188A, LY L1163A/Y2250A, NRY N1184A/R1185A/Y2250A. pEB, gray; WT CELSR1, purple; LF, teal; LY, brilliant green; NRY, light green. **c** The relative cell surface expression of each construct is presented as a fold change over wild type; points, error, and color as in (b). **d** Representative cell-cell aggregation assay images. Two cell populations were transfected with GFP and the noted constructs, or dsRed with Empty Vector,

and cells were imaged to assess aggregation. **e** Quantification of cell aggregation images as aggregation index.  $N = 4$  independent biological replicates, each with 6 technical replicates; each data point is a technical replicate. The average is plotted as a bar graph with standard deviation shown for the error bars. LF L1163A/F2188A, LY L1163A/Y2250A, NRY N1184A/R1185A/Y2250A. pEB, gray; WT CELSR1, purple; LF, teal; LY, brilliant green; NRY, light green. **f** Quantification of aggregation index normalized to the relative cell surface expression of each construct, points, error, and color as in (e). One-way ANOVA analysis with Tukey's correction for multiple comparisons was performed to assess statistical significance between CELSR constructs in (e, f). \*\*\*\* corresponds to  $p < 0.0001$ . Each construct was compared to each other construct for the statistical testing, but only certain comparisons are shown for clarity. Source data are provided as a Source Data file.

between CADH9 and GAIN from our cryo-EM structure. We designed three mutants targeting side chains that contribute to the interface: L1163A/F2188A (LF), L1163A/Y2250A (LY), and N1184A/R1185A/Y2250A (NRY). These mutants were tested for relative expression using fluorescence microscopy (Fig. 6a–c), and their relative expression was used to normalize the cell aggregation data. We then performed cell aggregation assays where either empty vector or CELSR1 constructs were co-transfected with fluorescent proteins (Fig. 6d–f). We found that all three mutant constructs induced significantly higher aggregation in our assay than WT CELSR1, suggesting that if the CADH9-GAIN CMM is disrupted, the adhesive potential of CELSR1 is increased. We tested these point mutants in our signaling assay and found that none of our mutants had altered signaling activity compared to WT CELSR1 (Supplementary Fig. 7).

## Discussion

CELSRs are highly conserved adhesion GPCRs critical for animal development<sup>4–6</sup>. Their large ECRs have remained enigmatic; their role in cellular adhesion, signaling, and other functions remains unclear, and molecular-level detail has been sparsely available. In this work, we determined the cryo-EM structure of the CELSR1 ECR, revealing a CMM containing CADH9-GAIN. We also used functional assays to define two modules of the protein; CADH1-8 is required for cellular adhesion, whereas CADH9-GAIN regulates cellular adhesion.

Our work adds a key structure to the landscape of the adhesion GPCRs by defining the three-dimensional structure of the CELSR/ADGRC ECR. The CADH9-GAIN region of CELSR1 contains 14 domains arranged in a CMM mediated by conserved hydrophobic contacts between the N-terminal CADH9 domain and the C-terminal GAIN domain. As such, the CADH9-GAIN CMM is likely present across CELSR/Flamingo orthologs. Our data provide molecular detail to a previous report showcasing low-resolution atomic force microscopy images of the full CELSR2 ECR<sup>57</sup>. The CADH9-GAIN CMM is large, with a solvent-accessible surface area of 71,000 Å<sup>2</sup>, and presents several putative ligand binding sites to the extracellular milieu, including the putative “hypervariable” surface of the LamG2 domain<sup>71</sup>. Others have suggested a role for this CADH9-GAIN CMM in the interaction of Fmi with Frizzled<sup>69</sup>, but the molecular details of this interaction, as well as the interaction of the known PCP ligands Frizzled and Van Gogh with CELSR1 in cis<sup>12</sup>, remain unclear. The CADH9-GAIN CMM of CELSR3 is the proposed binding site for  $\beta$ -amyloid oligomers<sup>82</sup>. Additionally, CELSR2 has been shown to dimerize in a parallel configuration via its globular CADH9-GAIN CMM, and this binding site remains to be determined<sup>57</sup>.

Evidence collected by us and others is consistent with a model of the CADH1-8 mediated antiparallel dimer driving the adhesive activity of CELSRs<sup>12,13,20,57,69</sup>. In the presence of Ca<sup>2+</sup>, we determined an extended species ~500 Å long from our SAXS data. We acknowledge that our

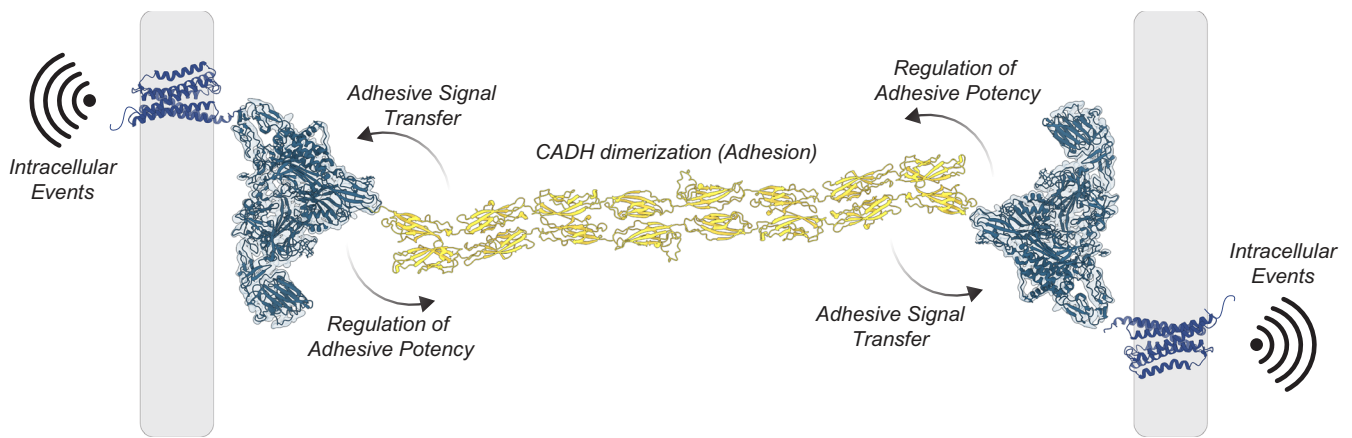


**Fig. 7 | Integrative model for ECR-mediated functions of CELSR1.** The dimerization of the cadherin repeat region, CADH1-8 (yellow), leads to cell aggregation and localization to the cell-cell junction. This adhesion can be regulated by the

CADH9-GAIN CMM (dark teal). The receptor (blue) can induce intracellular events in response to these adhesive events in the extracellular space. The model for the CADH1-8 dimer and the 7TM were generated using AlphaFold3<sup>83</sup>.

SAXS data taken alone do not allow us to distinguish between a fully extended dimer vs. bent or V-shaped dimers, or a mixture of these species. However, the preponderance of available evidence suggests an extended antiparallel dimer. A recent report, which used atomic force microscopy to determine low-resolution images of CELSR ECR constructs, observed an extended dimer species with the CADH repeats in a linear configuration<sup>57</sup>. In this model, each protomer is twisted around the other, where CADH1 interacts with CADH8 on the opposing monomer, CADH2 with CADH7, and so forth. This dimerization mode is similar to known protocadherin structures, where the cadherin repeats are arranged in an antiparallel fashion, and they twist around each other<sup>51–56</sup>. Additionally, AlphaFold3 predictions of the CELSR1 CADH1-8 dimer reveal a similar extended architecture (Fig. 7)<sup>83</sup>. We propose that this trans antiparallel dimer mediates the adhesive function of CELSR, as our deletion of the CADH1-8 module abrogates cell aggregation activity as well as the cell-cell junction localization of CELSR1 in cells. The use of EGTA disrupted WT CELSR1-mediated aggregation, also consistent with a  $\text{Ca}^{2+}$ -dependent antiparallel dimer of CADH repeats. These data are consistent with what others have found using the cell aggregation assay<sup>12,13,20</sup>, including a group which recently found that CADH1-8 of the CELSR homolog Fmi is necessary and sufficient for cell adhesion<sup>69</sup>. This tight multi-CADH dimer thus may be relevant to the role that CELSRs play in many processes which require the maintenance or coordinated change of cell-cell contacts in response to changes in force or pressure<sup>6,8,10,16,17</sup>. Future work will reveal the detailed molecular architecture of the CELSR antiparallel dimer, explaining the mechanism of how the known CELSR mutations Crash and Spin Cycle result in neuromuscular dysfunction<sup>8</sup>.

We propose that the CELSR1 CMM is the crucial structural feature of CELSR-subfamily aGPCRs (Fig. 7). Our data suggest that the CMM regulates the orientation and exposure of the adhesive CADH1-8 region in the extracellular space. For other adhesion molecule complexes, the rigidity of the ECR, the relative orientation between domains, is important for productive adhesion<sup>84</sup>. Point mutations in the CMM, which likely disrupt the CADH9/GAIN interface and could favor an extended CMM conformation, enhance CELSR1-mediated cell aggregation. This is consistent with a model proposed for Fmi, where binding of Frizzled to Fmi in cis results in a conformational change that enhances the CADH1-8 dimer in trans<sup>69</sup>. The ability of the CELSR CMM to transition between the compact conformation we observe in our cryo-EM structure and a putative extended conformation (driven by our point mutations or by a binding partner) may explain how the symmetric CADH1-8 dimer can be regulated in an asymmetric fashion in order to establish PCP. This is similar in principle to the closed/

compact and open/extended conformations observed for the ADGRG6 ECR, which are regulated by alternative splicing<sup>74</sup>. We speculate based on this work that aGPCRs, in general, may have N-terminal regions of their ECRs as adhesive regions and that the adhesive signal is communicated to a CMM, which can regulate this adhesive potential. Indeed, several aGPCRs employ their N-terminal domains to bind a protein ligand: ADGRL3 with TEN2 and FLRT<sup>60,85–87</sup>, ADGRG1 with transglutaminase 2<sup>88</sup>, and ADGRG6 with Collagen IV<sup>89</sup>. We add to this list CELSR1, which uses its N-terminal CADH repeats to mediate homophilic adhesion in trans. In each case, the N-terminus extends farthest away from the aGPCR-expressing cell, so it is poised to interact with ligands in the extracellular space. The adhesive “signal” can then be transferred to a CMM, the simplest version of which is the GAIN domain alone. Changes in CMM conformation could also dictate which binding partners could be recruited in cis, or binding partners in cis could change CMM conformation. It is also possible that this N-terminal adhesive signal operates through the CMM to regulate downstream receptor function<sup>90</sup>, although for CELSRs, it remains to be seen how signaling activity may relate to PCP function<sup>91</sup>.

Additionally, other aGPCRs have CMMs. ADGRG6 has 5 domains in a CMM mediated by its N-terminal CUB domain<sup>74</sup>. ADGRG1 has an N-terminal PLL domain, which is found tightly packed against its GAIN domain, generating a small, prototypic CMM<sup>92</sup>. In both ADGRG6 and ADGRG1, splice variants can disrupt these CMMs in order to regulate ligand binding and receptor function<sup>74,92,93</sup>. Overall, the intricate, modular architectures of aGPCRs likely evolved to withstand and react to strict spatial and force requirements in order to mediate intracellular events<sup>3,7,94–98</sup>. More experimental structures of aGPCRs with larger ECRs, such as ADGRV1, as well as comprehensive mechanistic studies including structural biology, adhesion, and functional readouts, will determine whether the CMM is a general structural feature of adhesion GPCRs.

## Methods

### Cloning and construct design

All amino acid numbering in this text is based on *M. musculus* CELSR1, UniProt entry O35161. Bioinformatic tools, including PROMALS3D<sup>99</sup>, SMART<sup>100</sup>, PSIPRED<sup>101</sup>, and CDD<sup>102</sup>, were used to identify domain boundaries and design CELSR1 constructs. The full-length CELSR1 and CELSR2 constructs in the pEB vector with N-terminal HA and C-terminal FLAG tags were previously described<sup>68</sup>. A region containing the CELSR1 CADH1 through GAIN domains (residues 255–2477) was amplified with these primers: F: 5'-CTGCCTTTGCGGCGAGCACCTC CCCACAGTCCCCCTGCC-3' and R: 5'-GTGGTGATGGTGATGATGATGATGCTCCCGTCTGCTTATGTC-3' and inserted into the pAcGP67a

vector with a C-terminal 8 × histidine tag using Gibson assembly<sup>103</sup>. The ΔCADH9-GAIN construct was generated with construct was generated using Gibson assembly by digesting the pEB backbone with EcoRV-HF and BamHI-HF (New England Biolabs) and inserting two Gibson fragments amplified using the following primers: 5'-cggatcgcagatcgttatcgaattcct-3' and 5'-actgccactaccgctgccCTGGTCCAGGAGACGGA TGT-3'; 5'-cagggcagcggtagtggtgacATTTCCAGACGTGAGCACG-3' and 5'-gccgctctagaactagtggatcc-3'. The ΔCADH1-8 construct was generated using Gibson assembly by digesting the pEB backbone with BamHI-HF (New England Biolabs) and inserting 3 Gibson fragments amplified using the following primers: 5'-aattcctgcagcccgggggatc-3' and 5'-agcatagtcaggtacatcataggggtaagcaactgcag-3', 5'-gatgtacctgactat gctTTGCCTGACTTCCAGATCCTTTTCAACAACTATG-3' and 5'-gCGTC ATTCATGTTTCAAGGTGGCaatgttg-3', 5'-GCCACCCTGAACATGAATGA CGc and 5'-gccgctctagaactagtggatccTCAttatcg-3'. The L1163/F2188 mutant was generated using pEB digested with BamHI and a four-part Gibson assembly using fragments generated with the following primers: 5'-aattcctgcagcccgggggatc-3' and 5'-cgggatccagcagcagcaag ctgcctcgttgcttgc-3', 5'-gcaaggcaacagggcagcgttgctgctggtgac-3' and 5'-gctgctaggtcagcgcctgctggcggc-3', 5'-gccgacagcagggcgctgacc tagcagcc-3' and 5'-gccgctctagaactagtggatccTCAttatcg-3'. The L1163/Y2250 mutant was generated using pEB digested with BamHI and a four-part Gibson assembly using fragments generated with the following primers: 5'-aattcctgcagcccgggggatc-3' and 5'-cgggatccagcagcagcaagctgcctcgttgcttgc-3', 5'-gcaaggcaacagggcagcgttgctgctggtgac-3' and 5'-ggtgacgatgacgaaggcctcagagcggtcctcttcac-3', 5'-gtgaa-gaggacgctctgagggccttcgtcatcgtc-3' and 5'-gccgctctagaactagtggatcc TCAttatcg-3'. The N1184/R1185/Y2250 mutant was generated using pEB digested with BamHI and a four-part Gibson assembly using fragments generated with the following primers: 5'-aattcctgca gcccggggggtc-3' and 5'-CATGAGCGCCTCCAGTGAgctgcGTTGTCCA-GATCCCGGCTGA-3', 5'-CAGCCGGGATCTGGACAACgagctCCACTGG AGGCGCTCATG-3' and 5'-ggtgacgatgacgaaggcctcagagcggtcctcttcac-3', 5'-gtgaagaggacgctctgagggccttcgtcatcgtc-3' and 5'-gccgctctagaac tagtggatccTCAttatcg-3'.

Cell culture

Sf9 cells (Thermo Fisher, 12659017) were cultured in SF900-III medium with 10% (v/v) FBS (Sigma-Aldrich, F0926) at 27 °C and transfected with plasmids and commercial baculovirus DNA (Expression Systems, 91-002) using Cellfectin II (Thermo Fisher, 10362100). Following transfection, initial baculoviral stocks were harvested and Sf9 cells were used to produce high-titer recombinant baculovirus. As previously described<sup>60</sup>, High Five cells (*Trichoplusia ni*, female, ovarian Thermo Fisher, B85502) were used for the production of recombinant proteins. High Five cells were cultured using Insect-Xpress medium (Lonza, 04351Q) with 10 μg/mL gentamicin at 27 °C. High Five cells (Thermo Fisher, B85502) were infected with baculovirus at 2.0 × 10<sup>6</sup> cells/mL and incubated at 27 °C with 120 rpm shaking for 72 h.

HEK293T mammalian cells (ATCC, CRL-3216) were used for cell aggregation assays similar to previously described<sup>79</sup> and were cultured in Dulbecco's modified Eagle's medium (DMEM; Gibco, 11965092) supplemented with 10 % FBS (Sigma-Aldrich, F0926) at 37 °C in 5 % CO<sub>2</sub>. HEK293T cells (ATCC #CRL-11268) were used for junctional enrichment studies. Cells for junctional enrichment were maintained in DMEM (Gibco Cat# 11995065) plus 10 % FBS (Gibco Cat# 16000044) and 1X Penicillin-Streptomycin (Corning Cat# MT30002CI) at 37 °C and 5 % CO<sub>2</sub> for a maximum of 20 passage numbers.

Protein expression and purification

As previously described<sup>60</sup>, media was harvested from High Five cell culture 72 h after baculovirus infection. The media was centrifuged at room temperature at 900 × g for 15 min. The supernatant was harvested, transferred to a beaker with stirring at room temperature, and the following were added: 50 mM Tris pH 8.0, 5 mM CaCl<sub>2</sub>, and 1 mM

NiCl<sub>2</sub> (final concentrations listed). After 30 min, the solution was centrifuged for 30 min at 8000 × g. The clarified supernatant was then incubated with nickel-nitriloacetic (Ni-NTA) resin (QIAGEN 30250) with stirring at room temperature for at least 3 h. A Büchner funnel was used to collect resin and wash using a buffer composed of 10 mM Tris pH 8.5, 150 mM NaCl (TBS) with 20 mM imidazole, and then the washed resin was transferred to a poly-prep chromatography column (Bio-Rad). The protein was eluted using TBS buffer plus 200 mM imidazole. Fractions containing desired protein were pooled and concentrated using a 100 kDa centrifugal concentrator (Amicon UFC810024) and loaded on gel filtration chromatography using a Superose 6 Increase 10/300 column (GE Healthcare) using the following buffer: 10 mM Tris pH 8.5, 150 mM NaCl, with the supplementation of 1 mM CaCl<sub>2</sub> as necessary.

SAXS data collection and processing

See Table 2 for data collection and processing statistics, as well as Supplementary Data Files 1 and 2. SAXS was performed at BioCAT (Beamline 18ID at the Advanced Photon Source, Chicago) with in-line SEC to separate sample from aggregates and other contaminants thus ensuring optimal sample quality and MALS, dynamic light scattering (DLS), and refractive index measurement (RI) for additional biophysical characterization (SEC-MALS-SAXS). The samples

Table 2 | Small-angle X-ray scattering data collection and data processing information

	CELSR1 ECR (no CaCl <sub>2</sub> )	CELSR1 ECR (1 mM CaCl <sub>2</sub> )
Data collection		
Date	2022/12/08 12:25	2022/12/08 17:56
Instrument	BioCAT (Sector 18, APS)	BioCAT (Sector 18, APS)
Experiment Type	SEC-MALS-SAXS	SEC-MALS-SAXS
Column	Superose 6 10/300 Increase	Superose 6 10/300 Increase
Buffer	10 mM Tris pH 8.5, 150 mM NaCl	10 mM Tris pH 8.5, 150 mM NaCl, 1 mM CaCl <sub>2</sub>
Temperature (°C)	22	22
Loaded Volume (μL)	250	250
Concentration (mg/mL)	0.9	1.04
Detector	Eiger2 XE 9M	Eiger2 XE 9M
Wavelength (Å)	1.033	1.033
Camera Length (m)	3.682	3.682
q-measurement range (1/Å)	0.0027–0.42	0.0027–0.42
Exposure time (s)	0.6	0.4
Exposure period (s)	1.0	1.0
Flow rate (mL/min)	0.6	0.6
Attenuation	None	None
RAW version	2.1.4	2.1.4
Notes	None	Mismatched sheath (No CaCl <sub>2</sub> )
Data processing		
Guinier R <sub>g</sub> (Å)	59.83 ± 0.23	161 ± 5.46
Guinier fit r <sup>2</sup>	0.99	0.899
Molecular Weight (Vp) (kDa)	392.4	599.4
Molecular Weight (Vc) (kDa)	328.0	276.1
GNOM IFT R <sub>g</sub> (Å)	61.89 ± 0.27	167 ± 3.76
GNOM IFT D <sub>max</sub> (Å)	225	675
GNOM χ <sup>2</sup>	1.433	1.188

were loaded on a Superose 6 Increase column (Cytiva) run by a 1260 Infinity II HPLC (Agilent Technologies) at 0.6 mL/min. The flow passed through (in order) the Agilent UV detector, a MALS detector and a DLS detector (DAWN Helios II, Wyatt Technologies), and an RI detector (Optilab T-rEX, Wyatt). The flow then went through the SAXS flow cell. The flow cell consists of a 1.0 mm ID quartz capillary with  $\sim 20\ \mu\text{m}$  walls. A coflowing buffer sheath is used to separate the sample from the capillary walls, helping prevent radiation damage<sup>104</sup>. Scattering intensity was recorded using an Eiger2 XE 9M (Dectris) detector, which was placed 3.6 m from the sample, giving access to a  $q$ -range of  $0.003\text{--}0.42\ \text{\AA}^{-1}$ .  $0.6\ \text{s}$  (no  $\text{CaCl}_2$ ) or  $0.4\ \text{s}$  ( $1\ \text{mM}\ \text{CaCl}_2$ ) exposures were acquired every  $1\ \text{s}$  during elution, and data were reduced using BioXTAS RAW 2.1.4<sup>105</sup>. Buffer blanks were created by averaging regions flanking the elution peak, and the entire series was buffer-subtracted. The buffer-subtracted series was analyzed using EFA within RAW and separated into individual scattering components, and the separated  $I(q)$  vs  $q$  curves were used for subsequent analyses. The GNOM and DENSS packages within RAW were used to calculate IFTs and electron density maps for each scattering component. Molecular weights and hydrodynamic radii were calculated from the MALS and DLS data, respectively, using the ASTRA 7 software (Wyatt).

### Cryo-EM data collection

$3.5\ \mu\text{L}$  purified CELSR1 CADH1-GAIN ( $3.0\ \text{mg/mL}$ ) was applied on glow-discharged holey carbon grids (Quantifoil R1.2/1.3, 300 mesh), and vitrified using a Vitrobot Mark IV (FEI Company). The specimen was visualized at the National Cryo-EM Facility using a Titan Krios electron microscope (FEI) operating at 300 kV and equipped with a K3 direct electron detector (Gatan, Inc.) with the Latitude software (Gatan, Inc.). Images were recorded with a nominal magnification of  $\times 81,000$  in super-resolution counting mode, corresponding to a pixel size of  $0.55\ \text{\AA}$  on the specimen level. To maximize data collection speed while keeping image aberrations minimal, image shift was used as an imaging strategy, using one data position per hole with six holes targeted in one template with one focus position. In total, 5826 images with defocus values in the range of  $-1.0$  to  $-2.0\ \mu\text{m}$  were recorded using a dose rate of  $6.2\ \text{electrons/s/physical pixel}$ . The total exposure time was set to  $2.5\ \text{s}$ , resulting in an accumulated dose of about  $50\ \text{electrons per \AA}^2$  and a total of  $50$  frames per movie stack. To improve resolution, a second dataset of 5550 micrographs was collected in exactly the same manner on the same microscope, and the two particle stacks were combined at the stage of 3D classification.

### Cryo-EM processing and model building

A visual representation of the data processing pipeline is available in Supplementary Fig. 2, and important values and statistics are available in Table 1. RELION 4.0 was used for the initial steps of data processing on each set of micrographs separately<sup>106</sup>. Stack images were subjected to beam-induced motion correction using MotionCor2 and binned to  $1.1\ \text{\AA/pixel}$ <sup>107</sup>. The motion-corrected micrographs were then imported into CryoSPARC 4.1.2<sup>108</sup>, where all subsequent data processing occurred. CTF parameters for each micrograph were estimated using Patch CTF. A total of  $2,129,894$  particles were picked using the Blob picker and subjected to reference-free two-dimensional classification to discard particles categorized in poorly defined classes. A refined set of  $162,975$  particles was used to train the Template picker, which generated  $1,794,239$  particles. Again, reference-free two-dimensional classification was used to discard particles categorized in poorly defined classes, and a final set of  $79,985$  particles was used in the Ab-Initio Reconstruction job with three classes, which generated three volumes. The same three volumes were used in heterogeneous refinement with a larger particle stack, combining picks from the Blob and Template pickers

(removing duplicates) to generate a higher quality volume. This volume had  $235,891$  particles associated with it, and these particles were used to train the Topaz picker, which picked  $1,040,008$  particles. Again, reference-free two-dimensional classification was used to discard particles categorized in poorly defined classes, and a final set of  $947,890$  particles was merged with the picks from Autopicking and Template picking, with duplicates removed. Three volumes were used in multiple rounds of heterogeneous refinement with merged particles until the map quality no longer improved, and Non-Uniform Refinement was used to obtain the final Coulomb potential map. Reported resolutions are based on the gold-standard Fourier shell correlation using the  $0.143$  criterion<sup>109</sup>. Model building started from the AlphaFold2 model of CADH9-GAIN, which was docked into the EM density map using Phenix, refined using the real-space refinement module in the Phenix software suite<sup>110</sup>, and then manually checked and adjusted residue-by-residue in an iterative fashion along with further real-space refinement to fit the density using COOT<sup>111</sup>. The final model contains residues 1113–2470, and the final model statistics are provided in Table 1.

### Structural analysis and sequence conservation analysis

Structural analysis and manual inspection of structures were performed using PyMOL version 2.4.1 (Schrodinger), and sequence analysis was done using PROMALS3D<sup>99</sup> and the ConSurf<sup>112</sup> server. ChimeraX was used to analyze cryo-EM density maps and generate figures<sup>113</sup>.

### Molecular dynamics simulations

The structure used for these simulations was previously determined by Tamilselvan and Sotomayor (PDB ID 7SZ8)<sup>88</sup>. Atoms missing from the crystal structure were added with Swiss PDB Viewer. The crystal structure of water and sodium ions were removed from the protein. Using GROMACS version 2022, CELSR1 CADH4-7 was placed in a  $8216.1\ \text{nm}^3$  rhombal dodecahedron with side length  $13.9\ \text{nm}$  and periodic boundary conditions, ensuring over  $1\ \text{nm}$  of solvent between the most distant atoms of 7SZ8 and the boundaries. The box was solvated with the TIP3P water model using gmx solvate, and  $\text{Na}^+$  and  $\text{Cl}^-$  counterions were added using gmx genion. The protein structure was minimized with the leapfrog integrator in step sizes of  $0.1\ \text{\AA}$  until the max force was smaller than  $1000\ \text{kJ mol}^{-1}\ \text{nm}^{-1}$ .

The system was then subjected to a two-phase equilibration in the NVT and NPT ensembles with protein atoms under harmonic position restraints. A  $100\ \text{ps}$  NVT equilibration was carried out with a step size of  $2\ \text{fs}$  at  $300\ \text{K}$  with the Berendsen thermostat using a  $0.1\ \text{ps}$  coupling constant, and solvent velocities were assigned from the Boltzmann distribution. NPT equilibration was also carried out with a step size of  $2\ \text{fs}$  for  $100\ \text{ps}$ , and at  $1\ \text{atm}$  with Parrinello-Rahman pressure coupling ( $2.0\ \text{ps}$  coupling constant) using velocities from the NVT ensemble. Simulations on the unrestrained protein were run in the NPT ensemble for  $1\ \mu\text{s}$  and a  $2\ \text{fs}$  step size. Long-range electrostatics were computed with PME with a  $1.6\ \text{\AA}$  Fourier spacing and  $10\ \text{\AA}$  cutoff. All simulations were run with the AMBER99SB-ILDN force field. Different simulation conditions were separately solvated, minimized, and equilibrated as above.

**Simulated systems.** The WT simulation was prepared as described above. The K533/T564 simulation was designed by aligning calcium-coordinating junctions (CADH 4-5 and CADH 6-7) to the CADH 5-6 junction. After alignment, K533E and T564D were changed to match the calcium coordination geometry of the canonical sites, and the two missing calcium ions were added into their respective positions to make a three-calcium interdomain junction between cadherins 5 and 6. The  $\Delta\text{Ca}^{2+}$  simulation was prepared by removing the calcium ion between CADH 5 and 6 from the WT protein. All simulations were performed with  $N=1$ .

**PCA and free energy landscape analysis.** Trajectories from the simulations were extracted for the alpha carbons (C $\alpha$ s) of each residue for each simulation. PCs of the C $\alpha$ s were calculated by concatenating all three simulation trajectories for each with gmx trjcat and diagonalizing the covariance matrix with gmx covar. Trajectories were projected onto essential gmx anaeg and were plotted and visualized with a homemade Python script. The fractions of variance  $f$  captured by PCs were checked to verify that the first two PCs captured most of the variance and verify the quality of the dimension reduction by computing Eq. (1):

$$f = \frac{\{\lambda_i\}_{1 \leq i \leq 3N}}{\text{tr}(C)} \quad (1)$$

where  $\{\lambda_i\}_{1 \leq i \leq 3N}$  is the set of  $3N$  eigenvalues for  $N$   $\alpha$ -carbons, and  $\text{tr}(C)$  is the trace of the covariate matrix. Hierarchical clustering of free energy landscape wells was performed by scipy.cluster in a homemade Python script using the Ward clustering method to minimize variance in the  $l^2$  norm. Cluster centroids  $c_i$  were computed by averaging the PC1 and PC2 coordinates of frames within each cluster using Eq. (2):

$$c_i = \frac{1}{N_i} \sum_{j \in \text{cluster } i} (\text{PC1}, \text{PC2})_j \quad (2)$$

where  $N_i$  is the number of frames in the  $i$ th cluster. We chose the frame from the simulations whose PC coordinates are closest by  $l^2$  norm and constructed the 3D structure as a linear combination of PC1 and PC2 using gmx anaeg.

### Cell aggregation assay

As previously described<sup>79</sup>, HEK293T cells (ATCC, CRL-3216) were seeded using a 6-well plate in 2 mL of DMEM supplemented with 10% FBS and incubated overnight at 37 °C. When the cells reached ~60 % confluency, they were co-transfected with 1  $\mu$ g each of either pCMV5 + GFP or dsRed, CELSR1 + GFP or dsRed, CELSR2 + GFP or dsRed, ADGRL3 + GFP, and TEN2 + dsRed and 5  $\mu$ L LipoD293T (SL100668; SignaGen Laboratories) or Eugene 6 (Promega E2691). Two days after transfection, the media was aspirated and the cells were washed with 1xPBS, detached with 1xPBS containing 1 mM EGTA, and supplemented with 15  $\mu$ L of 50 mg mL<sup>-1</sup> DNase IV (Sigma, D5025). The cells were resuspended by pipetting to create single-cell suspensions, transferred to a microcentrifuge tube, and an additional 15  $\mu$ L of DNase solution was added to each sample. Seventy microliters of cells expressing the indicated constructs were mixed in a 1:1 ratio in one well of a non-coated 24-well plate containing 360  $\mu$ L of DMEM supplemented with 10 % FBS, 20 mM CaCl<sub>2</sub> and 10 mM MgCl<sub>2</sub> or DMEM with 10 % FBS, 10 mM MgCl<sub>2</sub>, and 20 mM EGTA for 5 h at 126 rpm at 37 °C with 5% CO<sub>2</sub> and imaged using a Leica Fluorescence Microscope with a 5 $\times$  objective. The aggregation index at time = 5 h was calculated using ImageJ 1.52e. A value for particle area of 2–3 cells was set as a threshold based on negative control values. The aggregation index was calculated by dividing the area of particles exceeding this threshold by the total area occupied by all particles in the individual fields.

### Immunocytochemistry

Cover glass (#0, 12 mm, Carolina Biological Supply Company #633009) was placed into 24-well plates and coated for 2 h with 100  $\mu$ L of 50  $\mu$ g/mL poly-D-lysine (Gibco #A38904-01) in the 37 °C tissue culture incubator. Excess poly-D-lysine was removed, coverslips were washed 3 $\times$  with sterile ddH<sub>2</sub>O, and dried for 30 min. HEK293T cells were plated at  $1.5 \times 10^5$  cells/well in 0.5 mL complete DMEM. After 16–24 h, cells were transfected with the indicated experimental plasmid via TransIT-2020 (Mirus MIR5400) with a total of 0.5  $\mu$ g DNA amount/condition/well. After 48 h post-transfection, cells were washed briefly once with PBS, fixed with 4 % PFA (Electron

Microscopy Science Cat# 15714) with 4% sucrose in PBS for 20 min at 4 °C, and washed 3  $\times$  5 min in PBS. For surface receptor labeling of HA tag, samples were then transferred directly into blocking buffer (4% BSA (Sigma Cat# 10735086001) plus 3% normal goat serum (Jackson ImmunoResearch #005000121) in PBS) for 1 h. Samples were then labeled with HA tag primary antibody (anti-HA mouse, Covance Cat# MMS101R; 1:2000) diluted into blocking buffer for 2 h at room temperature. Samples were washed 3  $\times$  5 min with PBS, permeabilized with 0.2% Triton X-100 in PBS for 5 min at room temperature, and incubated in primary ZO-1 antibody (ZO-1 polyclonal rabbit antibody, Invitrogen #61-7300, 1:2,000) diluted into blocking buffer for 2 h at room temperature. Samples were subsequently washed 3  $\times$  5 min with PBS and incubated in fluorescently conjugated secondary antibodies (goat anti-mouse Alexa Fluor 488, Thermo Fisher #A11001, 1:1000; goat anti-rabbit Alexa Fluor 546, Thermo Fisher #A11010, 1:1,000) diluted into blocking buffer together with Phalloidin Alexa 647 (Thermo Fisher #A22287, 1:40 in methanol) for 30 min at room temperature. Samples were then washed three times in PBS and mounted on UltraClear microscope slides (Denville Scientific Cat# M1021) using 10  $\mu$ L ProLong Gold antifade reagent (Invitrogen, #P36930) per coverslip.

### Fluorescence microscopy

Images were acquired using a Nikon A1r resonant scanning Eclipse Ti2 HD25 confocal microscope with a 10 $\times$  (Nikon #MRD00105, CFI60 Plan Apochromat Lambda, N.A. 0.45), 20 $\times$  (Nikon #MRD00205, CFI60 Plan Apochromat Lambda, N.A. 0.75), and 60 $\times$  (Nikon #MRD01605, CFI60 Plan Apochromat Lambda, N.A. 1.4) objectives, operated by NIS-Elements AR v4.5 acquisition software. Laser intensities and acquisition settings were established for individual channels and applied to entire experiments. Junctional enrichment assay images were collected at 0.07  $\mu$ m/pixel resolution with 0.07  $\mu$ m z-step sizes, denoised, and deconvoluted with Richardson-Lucy 3D deconvolution. Image analysis was conducted with Nikon Elements. For the Junction Enrichment analysis, junction enrichment was calculated as a ratio between the corrected mean intensity at junctions (indicated by ZO-1) and the corrected total intensity of the cells in contact. Corrected mean intensities at the regions of interest were obtained by background from subtracting mean intensities of the empty vector condition.

### CELSR signaling assay

Signaling assays were performed as previously described<sup>74,90,114</sup>. HEK293 cells were co-transfected with 0.35  $\mu$ g CELSR DNA or empty vector, 0.35  $\mu$ g GloSensor reporter plasmid (Promega, E2301), 9 ng  $\beta$ 2 adrenergic receptor, and 2.8  $\mu$ L of the transfection reagent Eugene 6 (Promega, PRE2693). After a 24-h incubation, the transfected cells were detached and seeded (50,000 cells per well) in a white 96-well assay plate. Following another 24-h incubation, the DMEM was replaced with 100  $\mu$ L Opti-MEM (Gibco, 31985079) and incubated for 30 min. To each well was then added 1  $\mu$ L GloSensor substrate and 11  $\mu$ L FBS. Luminescence measurements were taken after 20 min to allow for equilibration.

### Statistical analysis

All statistical analysis was performed using GraphPad Prism 10. For the cell aggregation assays, cell-cell junction assays, and signaling assays, all experiments were performed in at least  $N=3$  independent experiments in at least triplicate. For all assays, the one-way ANOVA with Tukey's post hoc correction for multiple comparisons was used to assess statistical significance.

### Reporting summary

Further information on research design is available in the Nature Portfolio Reporting Summary linked to this article.

## Data availability

All data are available in the main text or the supplementary materials. The final model and cryo-EM data have been deposited into the Protein Data Bank under PDB ID [8VY2](#) and EMD ID [EMD-43644](#). Small-angle X-ray scattering data are available at SASBDB under the accession codes SASDVS7 and SASDVT7 [<https://www.sasbdb.org/data/SASDVS7/>] and [<https://www.sasbdb.org/data/SASDVT7/>]. Simulation data are available from the Figshare repository [<https://doi.org/10.6084/m9.figshare.28811603>]. Source Data are provided with this paper. Plasmids and other reagents are available upon request from the corresponding authors, D.A. and R.C.S. Source data are provided with this paper.

## References

- Hamann, J. et al. International union of basic and clinical pharmacology. XCIV. adhesion G protein-coupled receptors. *Pharmacol. Rev.* **67**, 338–367 (2015).
- Purcell, R. H. & Hall, R. A. Adhesion G protein-coupled receptors as drug targets. *Annu. Rev. Pharmacol. Toxicol.* **58**, 429–449 (2018).
- Araç, D. & Leon, K. Structure, function and therapeutic potential of adhesion GPCRs. in *GPCRs: Structure, Function, and Drug Discovery* 23–41. <https://doi.org/10.1016/B978-0-12-816228-6.00002-7> (2019).
- Boutin, C., Goffinet, A. M. & Tissir, F. Celsr1-3 cadherins in PCP and brain development. in *Current Topics in Developmental Biology* Vol. 101, 161–183 (Academic Press Inc., 2012).
- Tissir, F. & Goffinet, A. M. Atypical cadherins Celsr1-3 and planar cell polarity in vertebrates. in *Progress in Molecular Biology and Translational Science* Vol. 116, 193–214 (Elsevier B.V., 2013).
- Wang, X. J. et al. Understanding cadherin EGF LAG seven-pass G-type receptors. *J. Neurochem.* **131**, 699–711 (2014).
- Langenhan, T., Piao, X. & Monk, K. R. Adhesion G protein-coupled receptors in nervous system development and disease. *Nat. Rev. Neurosci.* **17**, 550–561 (2016).
- Curtin, J. A. et al. Mutation of Celsr1 disrupts planar polarity of inner ear hair cells and causes severe neural tube defects in the mouse. *Curr. Biol.* **13**, 1129–1133 (2003).
- Shi, D. et al. Celsr1 is required for the generation of polarity at multiple levels of the mouse oviduct. *Development* **141**, 4558–4568 (2014).
- Duncan, J. S. et al. Celsr1 coordinates the planar polarity of vestibular hair cells during inner ear development. *Dev. Biol.* **423**, 126–137 (2017).
- Devenport, D. & Fuchs, E. Planar polarization in embryonic epidermis orchestrates global asymmetric morphogenesis of hair follicles. *Nat. Cell Biol.* **10**, 1257–1268 (2008).
- Stahley, S. N., Basta, L. P., Sharan, R. & Devenport, D. Celsr1 adhesive interactions mediate the asymmetric organization of planar polarity complexes. *eLife* **10**, 1–26 (2021).
- Usui, T. et al. Flamingo, a seven-pass transmembrane cadherin, regulates planar cell polarity under the control of Frizzled. *Cell* **98**, 585–595 (1999).
- Nishimura, T., Honda, H. & Takeichi, M. Planar cell polarity links axes of spatial dynamics in neural-tube closure. *Cell* **149**, 1084–1097 (2012).
- Ravni, A., Qu, Y., Goffinet, A. M. & Tissir, F. Planar cell polarity cadherin Celsr1 regulates skin hair patterning in the mouse. *J. Invest. Dermatol.* **129**, 2507–2509. <https://doi.org/10.1038/jid.2009.84> (2009).
- Tissir, F. et al. Lack of cadherins Celsr2 and Celsr3 impairs ependymal ciliogenesis, leading to fatal hydrocephalus. *Nat. Neurosci.* **13**, 700–707 (2010).
- Tatin, F. et al. Planar cell polarity protein Celsr1 regulates endothelial adherens junctions and directed cell rearrangements during valve morphogenesis. *Dev. Cell* **26**, 31–44 (2013).
- Tissir, F., Bar, I., Jossin, Y. & Goffinet, A. M. Protocadherin Celsr3 is crucial in axonal tract development. *Nat. Neurosci.* **8**, 451–457 (2005).
- Zhou, L., Tissir, F. & Goffinet, A. M. The atypical cadherin Celsr3 regulates the development of the axonal blueprint. in *Cortical Development: Genes and Genetic Abnormalities* 130–134. <https://doi.org/10.1002/9780470994030.ch10> (John Wiley and Sons Ltd., 2008).
- Shima, Y., Kengaku, M., Hirano, T., Takeichi, M. & Uemura, T. Regulation of dendritic maintenance and growth by a mammalian 7-pass transmembrane cadherin. *Dev. Cell* **7**, 205–216 (2004).
- Qu, Y. et al. Atypical cadherins Celsr1-3 differentially regulate migration of facial branchiomotor neurons in mice. *J. Neurosci.* **30**, 9392–9401 (2010).
- Glasco, D. M. et al. The atypical cadherin Celsr1 functions non-cell autonomously to block rostral migration of facial branchiomotor neurons in mice. *Dev. Biol.* **417**, 40–49 (2016).
- Freitas, A. E., Gorodetski, L., Lim, W. L. & Zou, Y. Emerging roles of planar cell polarity proteins in glutamatergic synapse formation, maintenance and function in health and disease. *Dev. Dyn.* **252**, 1068–1076. <https://doi.org/10.1002/dvdy.574> (2023).
- Formstone, C. J. & Little, P. F. R. The flamingo-related mouse Celsr family (Celsr1-3) genes exhibit distinct patterns of expression during embryonic development. *Mech. Dev.* **109**, 91–94 (2001).
- Tissir, F., De-Backer, O., Goffinet, A. M. & Lambert de Rouvroit, C. Developmental expression profiles of Celsr (Flamingo) genes in the mouse. *Mech. Dev.* **112**, 157–160 (2002).
- Shima, Y. et al. Differential expression of the seven-pass transmembrane cadherin genes Celsr1-3 and distribution of the Celsr2 protein during mouse development. *Dev. Dyn.* **223**, 321–332 (2002).
- Formstone, C. J., Moxon, C., Murdoch, J., Little, P. & Mason, I. Basal enrichment within neuroepithelia suggests novel function(s) for Celsr1 protein. *Mol. Cell. Neurosci.* **44**, 210–222 (2010).
- Chen, Z. et al. Genetic analysis of Wnt/PCP genes in neural tube defects. *BMC Med. Genom.* **11**, 38 (2018).
- Qiao, X. et al. Genetic analysis of rare coding mutations of CELSR1-3 in congenital heart and neural tube defects in Chinese people. *Clin. Sci.* **130**, 2329–2340 (2016).
- Allache, R., De Marco, P., Merello, E., Capra, V. & Kibar, Z. Role of the planar cell polarity gene CELSR1 in neural tube defects and caudal agenesis. *Birth Defects Res. A Clin. Mol. Teratol.* **94**, 176–181 (2012).
- Robinson, A. et al. Mutations in the planar cell polarity genes CELSR1 and SCRIB are associated with the severe neural tube defect craniorachischisis. *Hum. Mutat.* **33**, 440–447 (2012).
- Lei, Y. et al. Identification of novel CELSR1 mutations in spina bifida. *PLoS ONE* **9**, e92207 (2014).
- Maltese, P. E. et al. Increasing evidence of hereditary lymphedema caused by CELSR1 loss-of-function variants. *Am. J. Med. Genet. A* **179**, 1718–1724 (2019).
- Smith, M. S., Sarasua, S. M., Rogers, C., Phelan, K. & Boccuto, L. Lymphedema is associated with CELSR1 in Phelan-McDermid syndrome. *Clin. Genet.* <https://doi.org/10.1111/cge.14364> (2023).
- Sudduth, C. L. et al. Primary upper extremity lymphedema caused by a CELSR1 variant. *J. Vasc. Anom.* **3**, e041 (2022).
- Gonzalez-Garay, M. L. et al. A novel mutation in CELSR1 is associated with hereditary lymphedema. *Vasc. Cell* **8**, 1 (2016).
- Seo, S. H. et al. Clinical staging and genetic profiling of Korean patients with primary lymphedema using targeted gene sequencing. *Sci. Rep.* **12**, 13591 (2022).
- Kaučká, M. et al. The planar cell polarity pathway drives pathogenesis of chronic lymphocytic leukemia by the regulation of b-lymphocyte migration. *Cancer Res.* **73**, 1491–1501 (2013).

39. Vilboux, T. et al. CELSR2, encoding a planar cell polarity protein, is a putative gene in Joubert syndrome with cortical heterotopia, microphthalmia, and growth hormone deficiency. *Am. J. Med. Genet. A* **173**, 661–666 (2017).
40. Willsey, A. J. et al. De novo coding variants are strongly associated with Tourette disorder. *Neuron* **94**, 486–499.e9 (2017).
41. de Koning, M. A. et al. De novo heterozygous missense variants in CELSR1 as cause of fetal pleural effusions and progressive fetal hydrops. *J. Med. Genet.* 1–4 <https://doi.org/10.1136/jmg-2023-109698> (2024).
42. Hulpiau, P. & Van Roy, F. New insights into the evolution of metazoan cadherins. *Mol. Biol. Evol.* **28**, 647–657 (2011).
43. Berger-Müller, S. & Suzuki, T. Seven-pass transmembrane cadherins: roles and emerging mechanisms in axonal and dendritic patterning. *Mol. Neurobiol.* **44**, 313–320 (2011).
44. Gul, I. S., Hulpiau, P., Saeys, Y. & van Roy, F. Evolution and diversity of cadherins and catenins. *Exp. Cell Res.* **358**, 3–9 <https://doi.org/10.1016/j.yexcr.2017.03.001> (2017).
45. Shapiro, L. & Weis, W. I. Structure and biochemistry of cadherins and catenins. *Cold Spring Harb. Perspect. Biol.* **1**, 1–21 (2009).
46. Honig, B. & Shapiro, L. Adhesion protein structure, molecular affinities, and principles of cell-cell recognition. *Cell* **181**, 520–535 (2020).
47. Leckband, D. E. & de Rooij, J. Cadherin adhesion and mechanotransduction. *Annu. Rev. Cell Dev. Biol.* **30**, 291–315 (2014).
48. De-la-Torre, P., Choudhary, D., Araya-Secchi, R., Narui, Y. & Sotomayor, M. A mechanically weak extracellular membrane-adjacent domain induces dimerization of protocadherin-15. *Biophys. J.* **115**, 2368–2385 (2018).
49. Hulpiau, P. & van Roy, F. Molecular evolution of the cadherin superfamily. *Int. J. Biochem. Cell Biol.* **41**, 349–369. <https://doi.org/10.1016/j.biocel.2008.09.027> (2009).
50. Tanoue, T. & Takeichi, M. New insights into fat cadherins. *J. Cell Sci.* **118**, 2347–2353 (2005).
51. Goodman, K. M. et al. Structural basis of diverse homophilic recognition by clustered  $\alpha$ - and  $\beta$ -protocadherins. *Neuron* **90**, 709–723 (2016).
52. Brasch, J. et al. Visualization of clustered protocadherin neuronal self-recognition complexes. *Nature* **569**, 280–283 (2019).
53. Harrison, O. J. et al. Family-wide structural and biophysical analysis of binding interactions among non-clustered  $\delta$ -protocadherins. *Cell Rep.* **30**, 2655–2671.e7 (2020).
54. Sotomayor, M., Weihofen, W. A., Weihofen, W. A. & Corey, D. P. Structure of a force-conveying cadherin bond essential for inner-ear mechanotransduction. *Nature* **492**, 128–132 (2012).
55. Rubinstein, R. et al. Molecular logic of neuronal self-recognition through protocadherin domain interactions. *Cell* **163**, 629–642 (2015).
56. Jaiganesh, A., Narui, Y., Araya-Secchi, R. & Sotomayor, M. Beyond cell-cell adhesion: sensational cadherins for hearing and balance. *Cold Spring Harb. Perspect. Biol.* **10**, a029280 (2018).
57. Nishiguchi, S., Kasai, R. S. & Uchihashi, T. Antiparallel dimer structure of CELSR cadherin in solution revealed by high-speed-atomic force microscopy. *Proc. Natl. Acad. Sci. USA* **120**, e2302047120 (2023).
58. Tamilselvan, E. & Sotomayor, M. CELSR1, a core planar cell polarity protein, features a weakly adhesive and flexible cadherin ecto-domain. *Structure* **32**, 1–16 (2024).
59. Li, J. et al. Structural basis for teneurin function in circuit-wiring: a toxin motif at the synapse. *Cell* **173**, 735–748.e15 (2018).
60. Li, J. et al. Alternative splicing controls teneurin-latrophilin interaction and synapse specificity by a shape-shifting mechanism. *Nat. Commun.* **11**, 2140 (2020).
61. Meijer, D. H., Frias, C. P., Beugeling, J. W., Deurloo, Y. N. & Janssen, B. J. C. Teneurin4 dimer structures reveal a calcium-stabilized compact conformation supporting homomeric trans-interactions. *EMBO J.* **41**, e107505 (2022).
62. Pavšič, M., Gunčar, G., Djinić-Carugo, K. & Lenarčič, B. Crystal structure and its bearing towards an understanding of key biological functions of EpCAM. *Nat. Commun.* **5**, 4764 (2014).
63. Chen, F., Venugopal, V., Murray, B. & Rudenko, G. The structure of neuexin 1 $\alpha$  reveals features promoting a role as synaptic organizer. *Structure* **19**, 779–789 (2011).
64. Gogou, C. et al. Alternative splicing controls teneurin-3 compact dimer formation for neuronal recognition. *Nat. Commun.* **15**, 3648 (2024).
65. Yamagata, A. et al. Structural insights into modulation and selectivity of transsynaptic neuexin–LRRTM interaction. *Nat. Commun.* **9**, 1–11 (2018).
66. Araç, D. et al. Structures of neuroligin-1 and the neuroligin-1/neuexin-1 $\beta$  complex reveal specific protein-protein and protein-Ca<sup>2+</sup> interactions. *Neuron* **56**, 992–1003 (2007).
67. Araç, D. et al. A novel evolutionarily conserved domain of cell-adhesion GPCRs mediates autoproteolysis. *EMBO J.* **31**, 1364–1378 (2012).
68. Bui, D. L. H. et al. The adhesion GPCRs CELSR1-3 and LPHN3 engage G proteins via distinct activation mechanisms. *Cell Rep.* **42**, 112552 (2023).
69. Strutt, H., Warrington, S., Madathil, A. C. K., Langenhan, T. & Strutt, D. Molecular symmetry breaking in the Frizzled-dependent planar polarity pathway. *Curr. Biol.* **33**, 5340–5354.e6 (2023).
70. Read, J. *From Alchemy to Chemistry* (Courier Corporation, 1995).
71. Rudenko, G., Hohenester, E. & Muller, Y. A. LG/LNS domains: multiple functions—one business end? *Trends Biochem. Sci.* **26**, 363–368 (2001).
72. Chug, H., Trakhanov, S., Hülsmann, B. B., Pleiner, T. & Görlich, D. Crystal structure of the metazoan Nup62–Nup58–Nup54 nucleoporin complex. *Science* **350**, 106–110 (2015).
73. Holm, L., Laiho, A., Törönen, P. & Salgado, M. DALI shines a light on remote homologs: one hundred discoveries. *Protein Sci.* **32**, 1–18 (2023).
74. Leon, K. et al. Structural basis for adhesion G protein-coupled receptor Gpr126 function. *Nat. Commun.* **11**, 194 (2020).
75. Mirdita, M. et al. ColabFold: making protein folding accessible to all. *Nat. Methods* **19**, 679–682 (2022).
76. Powers, R. E., Gaudet, R. & Sotomayor, M. A partial calcium-free linker confers flexibility to inner-ear protocadherin-15. *Structure* **25**, 482–495 (2017).
77. Tsukasaki, Y. et al. Giant cadherins Fat and Dachous self-bend to organize properly spaced intercellular junctions. *Proc. Natl. Acad. Sci. USA* **111**, 16011–16016 (2014).
78. Häussinger, D. et al. Calcium-dependent homoassociation of E-cadherin by NMR spectroscopy: changes in mobility, conformation and mapping of contact regions. *J. Mol. Biol.* **324**, 823–839 (2002).
79. Kordon, S. P. et al. Isoform- and ligand-specific modulation of the adhesion GPCR ADGRL3/Latrophilin3 by a synthetic binder. *Nat. Commun.* **14**, 635 (2023).
80. Inada, M., Izawa, G., Kobayashi, W. & Ozawa, M. 293 cells express both epithelial as well as mesenchymal cell adhesion molecules. *Int. J. Mol. Med.* **37**, 1521–1527 (2016).
81. Beutel, O., Maraspini, R., Pombo-García, K., Martin-Lemaitre, C. & Honigsmann, A. Phase separation of zonula occludens proteins drives formation of tight junctions. *Cell* **179**, 923–936.e11 (2019).
82. Feng, B. et al. Planar cell polarity signaling components are a direct target of  $\beta$ -amyloid-associated degeneration of glutamatergic synapses. *Sci. Adv.* **7**, eabh2307 (2021).
83. Abramson, J. et al. Accurate structure prediction of biomolecular interactions with AlphaFold 3. *Nature* **630**, 493–500 (2024).

84. Özkan, E. et al. Extracellular architecture of the SYG-1/SYG-2 adhesion complex instructs synaptogenesis. *Cell* **156**, 482–494 (2014).
85. Lu, Y. C. et al. Structural basis of latrophilin-FLRT-UNC5 interaction in cell adhesion. *Structure* **23**, 1678–1691 (2015).
86. del Toro, D. et al. Structural basis of teneurin-latrophilin interaction in repulsive guidance of migrating neurons. *Cell* **180**, 323–339.e19 (2020).
87. Jackson, V. A. et al. Structural basis of latrophilin-FLRT interaction. *Structure* **23**, 774–781 (2015).
88. Salzman, G. S., Zhang, S., Fernandez, C. G., Araç, D. & Koide, S. Specific and direct modulation of the interaction between adhesion GPCR GPR56/ADGRG1 and tissue transglutaminase 2 using synthetic ligands. *Sci. Rep.* **10**, 1–9 (2020).
89. Paavola, K. J., Sidik, H., Zuchero, J. B., Eckart, M. & Talbot, W. S. Type IV collagen is an activating ligand for the adhesion G protein-coupled receptor GPR126. *Sci. Signal.* **7**, 1–10 (2014).
90. Kordon, S. P. et al. Conformational coupling between extracellular and transmembrane domains modulates holo-adhesion GPCR function. *Nat. Commun.* **15**, 10545 (2024).
91. Basta, L. P. et al. Celsr1 and Celsr2 exhibit distinct adhesive interactions and contributions to planar cell polarity. *Front. Cell Dev. Biol.* **10**, 1064907 (2022).
92. Salzman, G. S. et al. Structural basis for regulation of GPR56/ADGRG1 by its alternatively spliced extracellular domains. *Neuron* **91**, 1292–1304 (2016).
93. Li, T. et al. A splicing isoform of GPR56 mediates microglial synaptic refinement via phosphatidylserine binding. *EMBO J.* **39**, 1–20 (2020).
94. Vizurraga, A., Adhikari, R., Yeung, J., Yu, M. & Tall, G. G. Mechanisms of adhesion G protein coupled receptor activation. *J. Biol. Chem.* <https://doi.org/10.1074/jbc.rev120.007423> (2020).
95. Wilde, C., Mitgau, J., Suchý, T., Schöneberg, T. & Liebscher, I. Translating the force—mechano-sensing GPCRs. *Am. J. Physiol. Cell Physiol.* **322**, C1047–C1060 (2022).
96. Fu, C. et al. Unveiling mechanical activation: GAIN domain unfolding and dissociation in adhesion GPCRs. *Nano Lett.* **23**, 9179–9186 (2023).
97. Zhong, B. L. et al. Piconewton forces mediate GAIN domain dissociation of the latrophilin-3 adhesion GPCR. *Nano Lett.* **23**, 9187–9194 (2023).
98. Mitgau, J. et al. The N terminus of adhesion G protein-coupled receptor GPR126/ADGRG6 as allosteric force integrator. *Front. Cell Dev. Biol.* **10**, 873278 (2022).
99. Pei, J., Kim, B. H. & Grishin, N. V. PROMALS3D: a tool for multiple protein sequence and structure alignments. *Nucleic Acids Res.* **36**, 2295–2300 (2008).
100. Letunic, I., Khedkar, S. & Bork, P. SMART: recent updates, new developments and status in 2020. *Nucleic Acids Res.* **49**, D458–D460 (2021).
101. Buchan, D. W. A. & Jones, D. T. The PSIPRED Protein Analysis Workbench: 20 years on. *Nucleic Acids Res.* **47**, W402–W407 (2019).
102. Wang, J. et al. The conserved domain database in 2023. *Nucleic Acids Res.* **51**, D384–D388 (2023).
103. Gibson, D. G. et al. Enzymatic assembly of DNA molecules up to several hundred kilobases. *Nat. Methods* **6**, 343–345 (2009).
104. Kirby, N. et al. Improved radiation dose efficiency in solution SAXS using a sheath flow sample environment. *Acta Crystallogr. D Struct. Biol.* **72**, 1254–1266 (2016).
105. Hopkins, J. B., Gillilan, R. E. & Skou, S. BioXTAS RAW: improvements to a free open-source program for small-angle X-ray scattering data reduction and analysis. *J. Appl. Crystallogr.* **50**, 1545–1553 (2017).
106. Kimanius, D., Dong, L., Sharov, G., Nakane, T. & Scheres, S. H. W. New tools for automated cryo-EM single-particle analysis in RELION-4.0. *Biochem. J.* **478**, 4169–4185 (2021).
107. Zheng, S. Q. et al. MotionCor2: anisotropic correction of beam-induced motion for improved cryo-electron microscopy. *Nat. Methods* **14**, 331–332 (2017).
108. Punjani, A., Rubinstein, J. L., Fleet, D. J. & Brubaker, M. A. CryoSPARC: algorithms for rapid unsupervised cryo-EM structure determination. *Nat. Methods* **14**, 290–296 (2017).
109. Rosenthal, P. B. & Henderson, R. Optimal determination of particle orientation, absolute hand, and contrast loss in single-particle electron cryomicroscopy. *J. Mol. Biol.* **333**, 721–745 (2003).
110. Liebschner, D. et al. Macromolecular structure determination using X-rays, neutrons and electrons: recent developments in Phenix. *Acta Crystallogr. D. Struct. Biol.* **75**, 861–877 (2019).
111. Emsley, P., Lohkamp, B., Scott, W. G. & Cowtan, K. Features and development of Coot. *Acta Crystallogr. D Biol. Crystallogr.* **66**, 486–501 (2010).
112. Ashkenazy, H. et al. ConSurf 2016: an improved methodology to estimate and visualize evolutionary conservation in macromolecules. *Nucleic Acids Res.* **44**, W344–W350 (2016).
113. Pettersen, E. F. et al. UCSF ChimeraX: structure visualization for researchers, educators, and developers. *Protein Sci.* **30**, 70–82 (2021).
114. Nazarko, O. et al. A comprehensive mutagenesis screen of the adhesion GPCR latrophilin-1/ADGRL1. *iScience* **3**, 264–278 (2018).

## Acknowledgements

We thank Dr. James R. Fuller, Dr. Minglei Zhao, and Dr. Navid Bavi for valuable discussion and advice regarding cryo-EM data processing and model building. We thank Dr. Marcos Sotomayor for valuable discussion regarding the manuscript. We thank Dr. Zhiqing Wang of the NCEF facility for assistance in cryo-EM data collection. This research was, in part, supported by the National Cancer Institute's National Cryo-EM Facility at the Frederick National Laboratory for Cancer Research under contract 75N91019D00024. We thank Dr. Maxwell Watkins and Dr. Jesse Hopkins for assistance in SAXS and MALS data collection and processing. This research used resources of the Advanced Photon Source, a U.S. Department of Energy (DOE) Office of Science User Facility operated for the DOE Office of Science by Argonne National Laboratory under Contract No. DE-AC02-06CH11357. BioCAT was supported by grant P30 GM138395 from the National Institute of General Medical Sciences of the National Institutes of Health. The mass photometry analysis was performed by the Biophysics Core in the Research Resources Center of the University of Illinois at Chicago. Software used in the project was installed and configured by SBGrid. The content is solely the responsibility of the authors and does not necessarily reflect the official views of the National Institute of General Medical Sciences or the National Institutes of Health. This research was supported by the following grants: National Institutes of Health Grant R35GM148412 to D.A., National Institutes of Health Grant F32GM142266 and K99GM157487 to S.J.B., National Institutes of Health Grant R00MH117235 to R.C.S., and the Alfred P. Sloan Foundation Sloan Research Fellowship to R.C.S.

## Author contributions

S.J.B., D.A., and R.C.S. conceptualized and designed the study and its methodology. S.J.B., K.G., S.P.K., T.S., E.E.D., and J.L. conducted the experimental investigations. S.J.B. designed the visualizations in the manuscript with help from S.P.K. and feedback from D.A. D.A. and R.C.S. supervised the work. S.J.B. wrote the original draft of the manuscript. S.J.B. revised and edited the manuscript with feedback from D.A., R.C.S., and S.P.K.

## Competing interests

The authors declare no competing interests.

## Additional information

**Supplementary information** The online version contains supplementary material available at <https://doi.org/10.1038/s41467-025-59319-8>.

**Correspondence** and requests for materials should be addressed to Richard C. Sando or Demet Araç.

**Peer review information** *Nature Communications* thanks Çağdaş Dağ, Arun Shukla, Jin-Peng Sun, and the other, anonymous, reviewer(s) for their contribution to the peer review of this work. A peer review file is available.

**Reprints and permissions information** is available at <http://www.nature.com/reprints>

**Publisher's note** Springer Nature remains neutral with regard to jurisdictional claims in published maps and institutional affiliations.

**Open Access** This article is licensed under a Creative Commons Attribution-NonCommercial-NoDerivatives 4.0 International License, which permits any non-commercial use, sharing, distribution and reproduction in any medium or format, as long as you give appropriate credit to the original author(s) and the source, provide a link to the Creative Commons licence, and indicate if you modified the licensed material. You do not have permission under this licence to share adapted material derived from this article or parts of it. The images or other third party material in this article are included in the article's Creative Commons licence, unless indicated otherwise in a credit line to the material. If material is not included in the article's Creative Commons licence and your intended use is not permitted by statutory regulation or exceeds the permitted use, you will need to obtain permission directly from the copyright holder. To view a copy of this licence, visit <http://creativecommons.org/licenses/by-nc-nd/4.0/>.

© The Author(s) 2025